Time-domain simulations of sound propagation in a flow duct with extended-reacting liners

Antoni Alomar, Didier Dragna, Marie-Annick Galland

Journal of Sound and Vibration 507 (2021) 116137

Contents lists available at ScienceDirect

Journal of Sound and Vibration

journal homepage: www.elsevier.com/locate/jsv

Time-domain simulations of sound propagation in a flow duct with extended-reacting liners

Antoni Alomar*, Didier Dragna, Marie-Annick Galland

Universite de Lyon, Ecole Centrale de Lyon, INSA Lyon, UCB Lyon 1, CNRS LMFA UMR 5509 36 Av Guy de Collongue, Ecully 69134, France

ARTICLE INFO

Article history:
Received 4 May 2020
Revised 7 March 2021
Accepted 13 April 2021
Available online 28 April 2021

Keywords:
Aeroacoustics
Extended-reacting liners
High-order time-domain simulation
Perforated sheet

ABSTRACT

A general methodology to simulate acoustic propagation in ducts with extended-reacting liners in the time domain is presented, including a generic perforated sheet on the air-material interface. The Linearized Euler Equations (LEE) with a mean flow profile are solved in the duct and the linearized equations on an equivalent fluid are solved in the liner material. The auxiliary differential equation method (ADE) is used to prevent the computation of convolution integrals, and leads to a formulation compatible with high-order numerical schemes. The methodology is illustrated for the case of liners consisting of rigid-frame porous materials and a prototype of locally-resonant acoustic metamaterials. A one-dimensional (1D) test case is first used to validate the algorithm and assess the numerical error. The numerical order of the algorithm is the expected one, independently of the interface, as long as the number of poles retained in the partial fraction expansions involved in the formulation is high enough. The algorithm is then applied to a realistic two-dimensional (2D) configuration in a duct with flow, and is used to illustrate the restrained validity of the locally-reacting approximation. Finally, the impact of the flow Mach number on the acoustic performance of porous and metamaterial extended-reacting liners is briefly assessed.

1. Introduction

Acoustic liners are commonly used to attenuate the fan and engine noise of commercial aircraft. Classical configurations based on SDOF or DDOF Helmholtz resonators are well suited for the tonal noise component, but their broadband performance remains limited. New liner configurations are currently being investigated for application to the future generation of airliners.

Extended-reacting liners consisting of porous materials with improved broadband capabilities are being considered [1–3]. Porous materials are known to be excellent broadband sound absorbers. Only their mechanical properties, the need of hydrophobic materials, and maybe its limited performance at low frequencies have limited their development and use in this domain of application. Another type of liners which are currently being investigated for aeronautical applications are metamaterial-based liners [4,5]. In particular, locally-resonant metamaterials are capable of absorbing sound at low frequencies using a small material depth, which is certainly an advantage compared to liners based on Helmholtz resonators or

* Corresponding author.
E-mail addresses: tonignasi@gmail.com (A. Alomar), didier.dragna@ec-lyon.fr (D. Dragna), marie-annick.galland@ec-lyon.fr (M.-A. Galland).

https://doi.org/10.1016/j.jsv.2021.116137

porous liners, that require large depths to attenuate low frequencies. This might be particularly interesting for the new generation of ultra-high bypass ratio turbofans. Mixed porous-metamaterial configurations (sometimes called 'metaporous') have also been investigated [6].

As opposed to locally-reacting liners, which behave as a surface impedance, extended-reacting liners require that the sound propagation within the material is computed simultaneously to the duct. This is accomplished defining the effective properties of the medium, which in general depend on the frequency (and on the propagation direction for anisotropic media). A number of semi-analytical and numerical models have been proposed in the literature to study the propagation of sound in ducts with porous materials, including the boundary element method [7], the finite element method [8], the point-collocation method [9] and the mode-matching method [10,11]. Here we propose a time-domain approach. Time-domain simulation is the natural choice to study transient propagation problems. The solution can be obtained with high accuracy at a low computational cost, using optimized high order finite-difference schemes [12,13] and low-storage high-order temporal schemes [14], by the finite-difference time-domain (FDTD) approach. Other advantages include the simple account for the nonlinearity of sound propagation and the nonlinearity of the material behavior, and for the spatial gradients of the mean flow or the liner properties. Besides, direct noise computations, in which the aerodynamic field and the acoustic field are solved at the same time, start to be performed in the literature for flows in a lined duct [15–17]. Such simulations require a time-domain formulation of the boundary conditions.

In general, the inverse Fourier transform of the frequency-domain equations with frequency-dependent effective density and compressibility leads to time-domain equations involving convolution integrals. The calculation of these integrals is computationally-expensive, and so various approaches have been proposed to either simplify them, or prevent their computation entirely. Simplified equations are obtained by considering low- and high-frequency asymptotics of the effective medium [18]. Further simplification of the material, for example by using Zwikker and Kosten's model [19] or Hamet and Bérengier model [20,21], allows a straightforward time-domain formulation without convolution integrals, at the expense of an inaccurate broadband description of the material [22]. Reformulating the equivalent fluid equations for the Wilson's relaxation model [23] allows a numerical evaluation of the convolution integrals, applicable in the entire frequency range but with the limitation of large storage requirements. The same reformulation was also applied for the Johnson-Champoux-Allard-Lafarge (JCAL) model [24]. The recursive convolution method [25], the Z-transform method [26] and the auxiliary differential equation method (ADE) [27] are three numerical methods developed for time-domain propagation of electromagnetic waves in dispersive media, that avoid the computation of convolution integrals. They have started to be used in acoustics. Thus, the ADE method [28] was applied for wave propagation in a porous medium for the Wilson's relaxation model. Recently, the Z-transform method [29] was employed on the full equivalent fluid equations, with an application to the JCAL model. As opposed to the other approaches, ADE allows not only to account for materials with frequency-dependent effective properties, but also to maintain a high-order accuracy in time [28], making it compatible with high-order numerical schemes. As a general method to obtain a time-domain formulation for the propagation of waves on linear dispersive media, ADE has been recently applied to locally-reacting acoustic metamaterials [30]. The ADE method is here proposed to compute accurately and efficiently the propagation of sound within the liner material.

Acoustic liners are usually covered with a perforated sheet or a wire mesh, with several purposes: to add additional dissipation through the perforates, to minimize the impact of the liner on the flow, and to protect the liner material from intense turbulence. In general, the thickness of the perforated plates is much smaller than the acoustic wavelength, which suggests an effective model based on a pressure jump. At low and moderate pressure levels the pressure jump varies linearly with the normal velocity through the perforates, defining an impedance. A first estimation of this impedance is obtained by assuming that it is a real constant, as only the real component is responsible for acoustic dissipation, and in a number of cases it varies slowly with frequency. However, an accurate modeling requires that the impedance is a complex-valued function of frequency [31,32]. The effect of a grazing flow over the perforates has also been addressed, leading to corrections of the perforate impedance [33,34]. In previous time-domain approaches of locally-reacting liners, the impedance of the perforated sheet is simply added to the impedance of the cavities, and a time-domain implementation of the impedance boundary can be used [35–37]. Here we propose the use of ADE to account for arbitrary perforated sheets in the context of extended-reacting liners.

The objectives of this study are two-fold. First, introducing a time-domain methodology to compute sound propagation in flow ducts with extended-reacting liners, including a generic perforated sheet at the air-material interface, and which is compatible with high-order low-dispersion low-dissipation schemes. And second, to showcase its applicability to the case of rigid-frame porous liners and a prototype of locally-resonant metamaterial.

The paper is organized as follows. Section 2 shows the lined duct configuration. Section 3 presents the formulation, including the equations in the flow duct, in the liner material and through the air-material interface. In Section 4 the various liner materials used are introduced. The validation against an analytical solution in a 1D test case, involving reflection and transmission at an interface between two semi-infinite media, is presented in Section 5. The numerical error of the FDTD algorithm introduced by the treatment of the liner material and interface is also evaluated. Finally, the application to the 2D lined duct with flow is presented in Section 6, including a validation against experimental results and an assessment of the validity of the locally-reacting approximation.

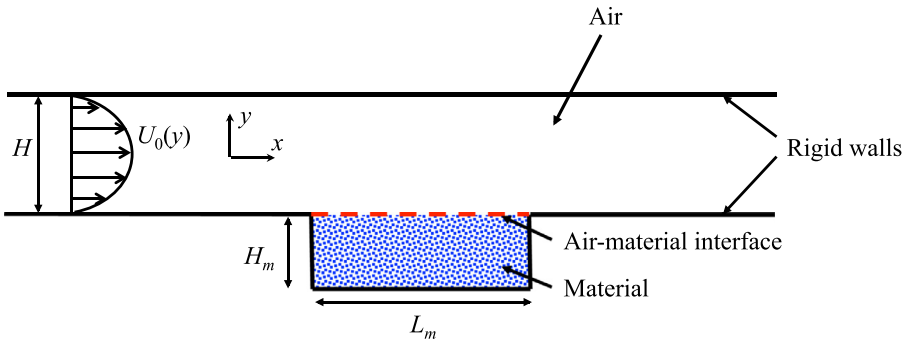

Fig. 1. Sketch of the geometry of the 2D lined duct.

2. Lined duct configuration

A two-dimensional (2D) straight duct of height H is considered, with a side cavity of length L_m and depth H_m filled with the liner material. A perforated sheet can be placed at the air-material interface. A sketch of the configuration is shown in Fig. 1. The duct can sustain a parallel mean flow with vanishing velocity on the rigid and lined walls.

3. Time-domain equations

3.1. In the flow duct

In the flow duct, small isentropic perturbations are assumed to propagate on an underlying mean parallel flow without density gradients and heat transfer. The Reynolds decomposition of the flow variables is:

$$P(x,y,t) = P_0 + p(x,y,t), \quad U(x,y,t) = U_0(y) + u(x,y,t), \quad V(x,y,t) = v(x,y,t), \tag{1}$$

where p, u and v are the perturbations of pressure, axial velocity and wall-normal velocity, respectively. Introducing them into the two-dimensional Euler equations and retaining only the linear terms in the perturbations lead to the following form of the Linearized Euler Equations (LEE):

$$\frac{\partial u}{\partial t} + U_0\frac{\partial u}{\partial x} + \frac{\mathrm{d}U_0}{\mathrm{d}y}v + \frac{1}{\rho_0}\frac{\partial p}{\partial x} = 0, \tag{2a}$$

$$\frac{\partial v}{\partial t} + U_0\frac{\partial v}{\partial x} + \frac{1}{\rho_0}\frac{\partial p}{\partial y} = 0, \tag{2b}$$

$$\frac{\partial p}{\partial t} + \rho_0 c_0^2\left(\frac{\partial u}{\partial x} + \frac{\partial v}{\partial y}\right) + U_0\frac{\partial p}{\partial x} = Q, \tag{2c}$$

where c_0 and ρ_0 are the mean sound speed and density, set to 340 m s^{-1} and 1.225 kg m^{-3}, respectively, and Q is a forcing term. The following model for the mean velocity profile is used:

$$U_0(y) = Mc_0\frac{n_y+1}{n_y}\left(1 - \left|1 - \frac{2y}{H}\right|^{n_y}\right) \tag{3}$$

where M is the flow Mach number defined through the bulk velocity, and n_y is a parameter directly related to the boundary layer displacement thickness. The displacement thickness has been set to 2% of the duct height throughout this study.

3.2. In the liner material

In order to obtain the time-domain equations, we start from the equations in the frequency domain, where the effective density and the inverse effective compressibility of the medium can be simply defined as functions of frequency (only isotropic materials are considered in this study). It is assumed there is no mean flow in the liner material. The equations governing sound propagation inside the material are (assuming all variables vary in time like $\mathrm{e}^{\mathrm{j}\omega t}$):

$$\mathrm{j}\omega\rho_e(\omega)\hat{u} + \frac{\partial \hat{p}}{\partial x} = 0, \tag{4a}$$

$$\mathrm{j}\omega\rho_e(\omega)\hat{v} + \frac{\partial \hat{p}}{\partial y} = 0, \tag{4b}$$

$$\mathrm{j}\omega C_e(\omega)\hat{p} + \frac{\partial \hat{u}}{\partial x} + \frac{\partial \hat{v}}{\partial y} = 0. \tag{4c}$$

The ADE method is used to transform the above equations to the time-domain. The effective density and compressibility are approximated by a partial fraction decomposition:

$$\rho_e(\omega) = \rho_{e\infty} + \sum_{k=1}^{Nr\rho} \frac{A_{\rho k}}{\lambda_{\rho k} + \mathrm{j}\omega} + \sum_{l=1}^{Ni\rho} \left(\frac{B_{\rho l} + \mathrm{j}C_{\rho l}}{\alpha_{\rho l} + \mathrm{j}\beta_{\rho l} + \mathrm{j}\omega} + \frac{B_{\rho l} - \mathrm{j}C_{\rho l}}{\alpha_{\rho l} - \mathrm{j}\beta_{\rho l} + \mathrm{j}\omega} \right), \tag{5a}$$

$$C_e(\omega) = C_{e\infty} + \sum_{k=1}^{NrC} \frac{A_{Ck}}{\lambda_{Ck} + \mathrm{j}\omega} + \sum_{l=1}^{NiC} \left(\frac{B_{Cl} + \mathrm{j}C_{Cl}}{\alpha_{Cl} + \mathrm{j}\beta_{Cl} + \mathrm{j}\omega} + \frac{B_{Cl} - \mathrm{j}C_{Cl}}{\alpha_{Cl} - \mathrm{j}\beta_{Cl} + \mathrm{j}\omega} \right). \tag{5b}$$

There exist various algorithms in the literature to determine the poles of the partial fraction expansions of given $\rho_e(\omega)$ and $C_e(\omega)$, such as vector fitting [38] or the Padé approximants [39]. In order that the solutions are stable all poles must have a positive real part, i.e. $\lambda_{\rho k}, \lambda_{Ck}, \alpha_{\rho k}, \alpha_{Ck} > 0$. This can be explicitly imposed in both methods. Vector fitting has been used throughout this study.

The partial fraction expansions of $\rho_e(\omega)$ and $C_e(\omega)$ can be obtained from an analytical model of the liner material, as done thereafter. It can also be directly extracted from measurements with an impedance tube, using the transfer function method [40]. This approach is of particular interest for novel acoustic materials, for which accurate analytical models are not yet available.

Introducing the partial fraction expansions of ρ_e and C_e into Eqs. (4a-4c), and taking the inverse Fourier transform leads to:

$$\rho_{e\infty}\frac{\partial u}{\partial t} + \sum_k A_{\rho k}\phi^x_{\rho k} + 2\sum_l \left(B_{\rho l}\psi^{xr}_{\rho l} + C_{\rho l}\psi^{xi}_{\rho l}\right) + \left(\sum_k A_{\rho k} + 2\sum_l B_{\rho l}\right)u + \frac{\partial p}{\partial x} = 0, \tag{6a}$$

$$\rho_{e\infty}\frac{\partial v}{\partial t} + \sum_k A_{\rho k}\phi^y_{\rho k} + 2\sum_l \left(B_{\rho l}\psi^{yr}_{\rho l} + C_{\rho l}\psi^{yi}_{\rho l}\right) + \left(\sum_k A_{\rho k} + 2\sum_l B_{\rho l}\right)v + \frac{\partial p}{\partial y} = 0, \tag{6b}$$

$$C_{e\infty}\frac{\partial p}{\partial t} + \sum_k A_{Ck}\phi_{Ck} + 2\sum_l \left(B_{Cl}\psi^r_{Cl} + C_{Cl}\psi^i_{Cl}\right) + \left(\sum_k A_{Ck} + 2\sum_l B_{Cl}\right)p + \left(\frac{\partial u}{\partial x} + \frac{\partial v}{\partial y}\right) = 0, \tag{6c}$$

where the auxiliary functions $\phi^x_{\rho k}, \phi^y_{\rho k}, \phi_{Ck}$ come from the real poles, and $\psi^{xr}_{\rho l}, \psi^{yr}_{\rho l}, \psi^{xi}_{\rho l}, \psi^{yi}_{\rho l}, \psi^r_{Cl}, \psi^i_{Cl}$ come from the complex conjugate poles. All of them are defined as convolution integrals of the form:

$$\phi^x_{\rho k} = \int_0^t \frac{\partial u}{\partial t} \exp[-\lambda_{\rho k}(t-\tau)]\,\mathrm{d}\tau - u,$$

which can be transformed through time derivation to the following set of partial differential equations:

$$\frac{\partial \phi^x_{\rho k}}{\partial t} + \lambda_{\rho k}\phi^x_{\rho k} + \lambda_{\rho k}u = 0, \quad k = 1, ..., Nr\rho \tag{7a}$$

$$\frac{\partial \phi^y_{\rho k}}{\partial t} + \lambda_{\rho k}\phi^y_{\rho k} + \lambda_{\rho k}v = 0, \quad k = 1, ..., Nr\rho \tag{7b}$$

$$\frac{\partial \phi_{Ck}}{\partial t} + \lambda_{Ck}\phi_{Ck} + \lambda_{Ck}p = 0, \quad k = 1, ..., NrC \tag{7c}$$

$$\frac{\partial \psi^{xr}_{\rho l}}{\partial t} + \alpha_{\rho l}\psi^{xr}_{\rho l} + \beta_{\rho l}\psi^{xi}_{\rho l} + \alpha_{\rho l}u = 0, \quad l = 1, ..., Ni\rho \tag{7d}$$

$$\frac{\partial \psi^{xi}_{\rho l}}{\partial t} + \alpha_{\rho l}\psi^{xi}_{\rho l} - \beta_{\rho l}\psi^{xr}_{\rho l} - \beta_{\rho l}u = 0, \quad l = 1, ..., Ni\rho \tag{7e}$$

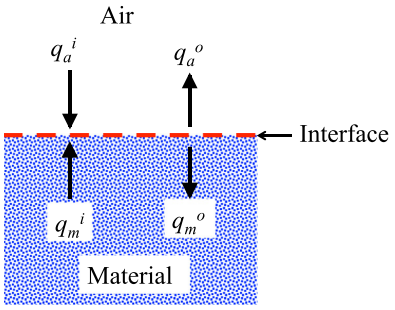

Fig. 2. Characteristics traveling towards the interface and away from the interface, in the air side and the material side.

$$\frac{\partial \psi_{\rho l}^{yr}}{\partial t} + \alpha_{\rho l}\psi_{\rho l}^{yr} + \beta_{\rho l}\psi_{\rho l}^{yi} + \alpha_{\rho l} v = 0, \quad l = 1, ..., Ni\rho \tag{7f}$$

$$\frac{\partial \psi_{\rho l}^{yi}}{\partial t} + \alpha_{\rho l}\psi_{\rho l}^{yi} - \beta_{\rho l}\psi_{\rho l}^{yr} - \beta_{\rho l} v = 0, \quad l = 1, ..., Ni\rho \tag{7g}$$

$$\frac{\partial \psi_{Cl}^{r}}{\partial t} + \alpha_{Cl}\psi_{Cl}^{r} + \beta_{Cl}\psi_{Cl}^{i} + \alpha_{Cl} p = 0, \quad l = 1, ..., NiC \tag{7h}$$

$$\frac{\partial \psi_{Cl}^{i}}{\partial t} + \alpha_{Cl}\psi_{Cl}^{i} - \beta_{Cl}\psi_{Cl}^{r} - \beta_{Cl} p = 0, \quad l = 1, ..., NiC \tag{7i}$$

3.3. Air-material interface

The air and the material have their own specific equations and computational domains. In order to transmit information between the two domains, the air-material interface is treated through the characteristic variables. Note that a comparable approach has been recently proposed for a frequency-dependent transmission boundary condition [41]. As opposed to the original variables, the characteristic variables have a well-defined propagation direction. This way, the condition that the perturbations traveling away from the interface are determined only from the perturbations traveling towards the interface can be explicitly imposed. A sketch of the characteristics in the air side and in the material side is shown in Fig. 2.

The incoming characteristics, traveling towards the interface from the air side and the liner material side, are, respectively:

$$q_a^i = p_a - \rho_0 c_0 v_a, \tag{8a}$$

$$q_m^i = p_m + \rho_{e\infty} c_{e\infty} v_m. \tag{8b}$$

where $(p_a,\ v_a)$ and $(p_m,\ v_m)$ are the acoustic pressure and normal velocity at the interface from the air side and liner material side, respectively and $c_{e\infty} = (\rho_{e\infty} C_{e\infty})^{-1/2}$ is the high-frequency limit of the sound speed in the material . Note that the wall normal is pointing away from the liner. Similarly, the outgoing characteristics, traveling away the interface from the air side and the liner material side, are, respectively:

$$q_a^o = p_a + \rho_0 c_0 v_a, \tag{9a}$$

$$q_m^o = p_m - \rho_{e\infty} c_{e\infty} v_m. \tag{9b}$$

The outgoing characteristics are then updated from the incoming ones, using the interface properties. Three cases are considered:

- In the case of a free interface, the pressure and normal velocity are continuous across the interface. One can then express the outgoing characteristics as a function of the incoming ones with the relations:

$$q_a^o = \frac{\rho_{e\infty} c_{e\infty} - \rho_0 c_0}{\rho_0 c_0 + \rho_{e\infty} c_{e\infty}} (q_a^i - q_m^i) + q_m^i, \tag{10a}$$

$$q_m^o = \frac{\rho_0 c_0 - \rho_{e\infty} c_{e\infty}}{\rho_0 c_0 + \rho_{e\infty} c_{e\infty}} (q_m^i - q_a^i) + q_a^i. \tag{10b}$$

- When there is a purely resistive screen a pressure jump exists at the interface, $p_a - p_m = R_{sh} v$, while the normal velocity is continuous, $v_a = v_m = v$. The outgoing characteristics are now:

$$q_a^o = \frac{R_{sh} + \rho_{e\infty} c_{e\infty} - \rho_0 c_0}{R_{sh} + \rho_0 c_0 + \rho_{e\infty} c_{e\infty}} (q_a^i - q_m^i) + q_m^i, \tag{11a}$$

$$q_m^o = \frac{R_{sh} + \rho_0 c_0 - \rho_{e\infty} c_{e\infty}}{R_{sh} + \rho_0 c_0 + \rho_{e\infty} c_{e\infty}} (q_m^i - q_a^i) + q_a^i. \tag{11b}$$

- Finally, in the case of a perforated plate characterized by a frequency-dependent complex impedance $Z_{sh}(\omega)$, the outgoing characteristics are, in the frequency domain:

$$\hat{q}_a^o = \frac{Z_{sh}(\omega) + \rho_{e\infty} c_{e\infty} - \rho_0 c_0}{Z_{sh}(\omega) + \rho_0 c_0 + \rho_{e\infty} c_{e\infty}} (\hat{q}_a^i - \hat{q}_m^i) + \hat{q}_m^i = K_{sh1}(\omega)(\hat{q}_a^i - \hat{q}_m^i) + \hat{q}_m^i, \tag{12a}$$

$$\hat{q}_m^o = \frac{Z_{sh}(\omega) + \rho_0 c_0 - \rho_{e\infty} c_{e\infty}}{Z_{sh}(\omega) + \rho_0 c_0 + \rho_{e\infty} c_{e\infty}} (\hat{q}_m^i - \hat{q}_a^i) + \hat{q}_a^i = K_{sh2}(\omega)(\hat{q}_m^i - \hat{q}_a^i) + \hat{q}_a^i. \tag{12b}$$

Similarly to what has been done with $\rho_e(\omega)$ and $C_e(\omega)$, partial fraction expansions of K_{sh1} and K_{sh2} are used to obtain the time-domain interface conditions:

$$K_{sh1} = K_{\infty 1} + \sum_k^{Nint} \frac{A_{K1k}}{\lambda_{K1k} + \mathrm{j}\omega},$$

$$K_{sh2} = K_{\infty 2} + \sum_k^{Nint} \frac{A_{K2k}}{\lambda_{K2k} + \mathrm{j}\omega}.$$

Introducing these into Eq. (12) we obtain

$$q_a^o = K_{\infty 1}(q_a^i - q_m^i) + \sum_k A_{K1k}\phi_{K1k} + q_m^i, \tag{14a}$$

$$q_m^o = K_{\infty 2}(q_m^i - q_a^i) + \sum_k A_{K2k}\phi_{K2k} + q_a^i, \tag{14b}$$

and the auxiliary equations for the interface are

$$\frac{\mathrm{d}\phi_{K1k}}{\mathrm{d}t} + \lambda_{K1k}\phi_{K1k} = q_a^i - q_m^i, \quad k = 1, ..., Nint, \tag{15a}$$

$$\frac{\mathrm{d}\phi_{K2k}}{\mathrm{d}t} + \lambda_{K2k}\phi_{K2k} = q_m^i - q_a^i, \quad k = 1, ..., Nint. \tag{15b}$$

The functions ϕ_{K1k} and ϕ_{K2k} are the auxiliary functions of the interface. Similarly to the effective density and effective compressibility, the functions K_{sh1} and K_{sh2} are fitted using a partial fraction expansion with a prescribed number of poles. In this case only real poles are considered due to the dissipative nature of the perforated plate, but a generalization to complex-conjugate pole pairs is straightforward.

Once the outgoing characteristic variables are updated depending on the interface properties (with Eq. (10), (11) or (12)) the pressure and the wall-normal velocity at each side of the interface are corrected with the relations

$$p_a = \frac{1}{2}(q_a^o + q_a^i), \qquad v_a = \frac{1}{2\rho_0 c_0}(q_a^o - q_a^i), \qquad p_m = \frac{1}{2}(q_m^o + q_m^i), \qquad v_m = \frac{1}{2\rho_{e\infty} c_{e\infty}}(q_m^i - q_m^o), \tag{16}$$

that are obtained from Eqs. (8) and (9).

3.4. Numerical schemes

Equations (2a -2c), (6a-6c), (7a-7i), (14a-14b) and (15a-15b) are integrated in time using the low-storage six-stage fourth-order Runge-Kutta scheme, denoted by RK46-L in [14]. The spatial derivatives are computed using optimized eleven-points fourth-order finite differences schemes. In detail, the centered scheme FDo11p proposed in [12] is used for the interior points, and the noncentered schemes FD_{010}, FD_{19}, FD_{28}, FD_{37} and FD_{46} proposed in [13] are employed for the interface and boundary points. In order to prevent grid-to-grid numerical instabilities, optimized selective filters are used. For the interior points, the centered eleven-points sixth-order filter proposed in [42] is used and at the interface and the boundaries of the domain, the second-order selective filters SF_{03}, SF_{15}, SF_{28}, SF_{37} and SF_{46} proposed in [13] are employed. In the 2D configuration, anechoic inlet and outlet sections are achieved through sponge zones [43], including non-reflecting boundary conditions [44]. The sponge zones extend 1 m upstream and 1 m downstream. The grid size in the central region of the duct, including the lined section, is uniform along the x-axis, and it decreases in the y direction towards the walls with a stretching factor of 0.99. A total of 65 grid points have been used across the main duct section, corresponding to $\mathrm{d}y = 3.6 \cdot 10^{-4}$ m on the duct axis and $\mathrm{d}y = 2.6 \cdot 10^{-4}$ m on the walls. The grid size in the x direction is then $\mathrm{d}x = 3.6 \cdot 10^{-4}$ m. The grid size in the liner cavity is uniform in both directions, and is such that it is continuous at the air-material interface. The filtering strength is set to 1 for all selective filters, except for the totally off-centered selective filter SF_{03} for which the filtering strength is reduced to 0.1. In all cases the CFL (Courant-Fridrichs-Lewy) number is limited to 0.75, which corresponds to a timestep of $\mathrm{d}t = 0.6 \cdot 10^{-6}$ s, and the total simulation time is 0.02 s.

Besides, to ensure a stable simulation, some conditions on the value of the poles should be also fulfilled. Indeed, the ADE equations have the general form: $\mathrm{d}u/\mathrm{d}t + \lambda u = 0$, neglecting any source term. When solving numerically this equation, $-\lambda$ should be in the stability region of the time-integration scheme to have a stable simulation [45]. The values of $\lambda\,\mathrm{d}t$, $\alpha\,\mathrm{d}t$ and $\beta\,\mathrm{d}t$ for ρ_e, C_e, K_{sh1} and K_{sh2} should then not be too large. For the Runge-Kutta algorithm employed here, a maximal value of 4 is a good rule of thumb.

The procedure to advance the FDTD algorithm in time for the general case is the following:

1. compute the spatial gradients of p, u, v throughout the domain
2. update fields of the flow variables, p, u, v, the auxiliary functions in the material, $\phi_{\rho k}$, ϕ_{Ck}, $\psi_{\rho l}$, ψ_{Cl}, and the auxiliary functions of the interface, ϕ_{K1k}, ϕ_{K2k}
3. compute the incoming characteristics at the interface q_a^i, q_m^i with Eq. (8)
4. compute the outgoing characteristics at the interface q_a^o, q_m^o with Eqs. (10), (11) or (12) depending on the interface properties
5. compute the values of p_m, v_m, p_a, v_a at the interface from the incoming and outgoing characteristics with Eq. (16) and impose zero wall-normal velocity on the rigid walls

4. Sound-absorbing materials and interfaces

The models for the materials and interfaces used hereafter are briefly presented. Concerning sound-absorbing materials, two types are considered: rigid-frame porous materials described by the Johnson-Champoux-Allard semiphenomenological model (JCA) [46], and prototypical models describing locally-resonant acoustic metamaterials. Both types of material allow a description of sound propagation using an equivalent fluid approach.

4.1. Rigid-frame porous materials

The proposed numerical methodology has been applied to two different rigid-frame porous materials described by JCA. For completeness, the equations for the effective density and compressibility in JCA are summarized in Appendix A. The model parameters are presented in Table 1. Note that the resistivity, σ, is equivalent to the viscous permeability through $k_0 = \mu/\sigma$, where μ is the dynamic viscosity. The fit using a partial fraction expansion is equally applicable to the JCAL model or the Johnson-Champoux-Allard-Pride-Lafarge (JCAPL) model if a more accurate description of the material is required. It has been checked that the low- and high-frequency limits of the partial fraction expansions match the limits of the JCA model. In particular, the divergent behavior of ρ_e at $\omega \to 0$ is naturally described by one real pole with $\lambda_\rho \approx 0$.

The error of the rational functions that approximate $\rho_e(\omega)$ and $C_e(\omega)$ (Eqs. (5a-5b)) diminishes fast with the number of poles. The vector fitting algorithm selects automatically real poles only to describe the porous materials, as expected for purely dissipative media. Fig. 3 shows the root-mean-square errors for both the aluminum foam and the polyurethane foam.

Table 1
JCA parameters of the porous materials considered.

Porous material	ϕ	α_∞	Λ (m)	Λ' (m)	σ (N·s·m^{-4})
Polyurethane foam	0.98	1.04	$2.0{\cdot}10^{-4}$	$5.0{\cdot}10^{-4}$	2850
Aluminum foam	0.645	2.25	$1.0{\cdot}10^{-4}$	$3.5{\cdot}10^{-4}$	19700

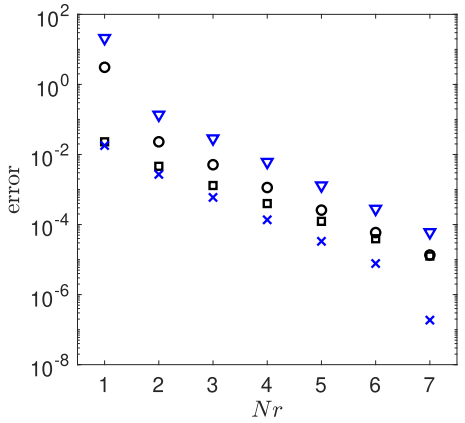

Fig. 3. Truncation error of the partial fraction expansions of ρ_e for the polyurethane foam (○) and the aluminum foam (▽), and of C_e for the polyurethane foam (□) and the aluminum foam (×).

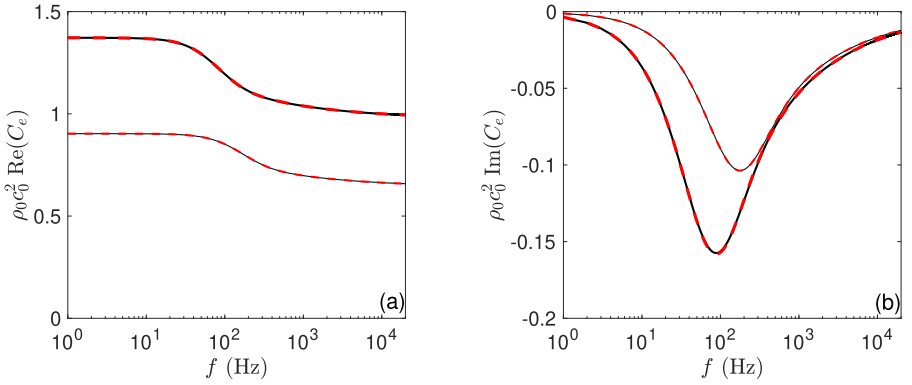

Fig. 4. (a) Real component and (b) imaginary component of the effective compressibility of the polyurethane foam (——) and the aluminum foam (——), together with the approximation using 5 real poles (- - - and - - -, respectively).

The error for ρ_e is computed as (an analogous expression applies to C_e):

$$\text{error} = \sqrt{\frac{\sum_n \left(\rho_e^{\text{JCA}}(\omega_n) - \rho_e(\omega_n)\right)^2}{\sum_n \rho_e^{\text{JCA}}(\omega_n)^2}},$$

where ρ_e^{JCA} is the effective density obtained from JCA, and ρ_e is its approximation using a rational function. The frequency vector is set to $\omega_n = 2\pi f_n$, with $f_n = 1, 2, 3, \ldots 20000$ Hz. Overall, the error diminishes exponentially with Nr, but with a rate that differs between ρ_e and C_e and also between the materials. At a visual level, no improvement can be detected for $Nr > 4$. Fig. 4 shows $C_e(\omega)$ corresponding to the polyurethane foam and the aluminum foam and the fits using 5 real poles.

4.2. Locally-resonant acoustic metamaterials

Acoustic metamaterials have attracted the attention of researchers as well as manufacturers during the last two decades, since it was shown experimentally that materials with negative effective density and/or effective compressibility (real parts) can exist and can be manufactured [47]. In particular, the so-called locally-resonant acoustic metamaterials, characterized by an acoustic wavelength much larger than the microstructure size, allow the approximation of sound propagation through them using effective models. Using effective medium theory several models have been deduced for the effective medium around the local resonances. A widely used model is a continuous distribution of local harmonic oscillators leading to an effective compressibility of the form [48–51]:

$$\frac{\rho_0 c_0^2 C_e(\omega)}{\phi} \approx 1 - \frac{F_C \omega_{*C}^2}{\omega^2 - \omega_{*C}^2 - \mathrm{j}\Gamma_C \omega}, \tag{17}$$

where ω_{*C} and Γ_C are the natural resonance frequencies of the effective medium and their damping coefficients, respectively. The porosity of the metamaterial has been included in the model, which allows a deviation of the high-frequency limit with

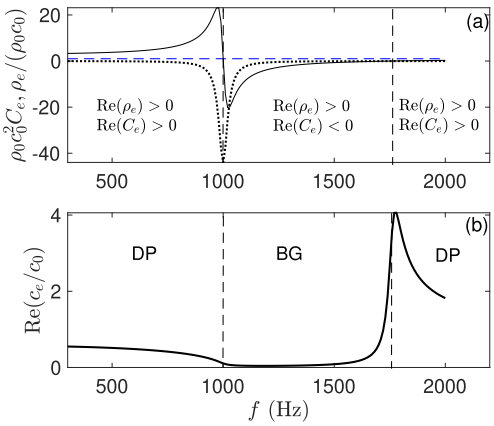

Fig. 5. (a) Real effective density (- - -), real effective compressibility (——) and imaginary effective compressibility (.....) of a metamaterial with a local resonance of the effective compressibility at 1000 Hz; (b) effective sound speed.

Table 2
Parameters of the perforated plates.

Perforated sheet	ϕ_{sh}, porosity	e, thickness (mm)	d, hole diameters (mm)
PS1	0.2	0.5	2.0
PS2	0.05	2	0.4

respect to the density and compressibility of ambient air. An analogous expression can be supposed for the effective density:

$$\frac{\phi \rho_e(\omega)}{\rho_0} \approx 1 - \frac{F_\rho \omega_{*\rho}^2}{\omega^2 - \omega_{*\rho}^2 - \mathrm{j}\Gamma_\rho \omega}. \tag{18}$$

Time-domain simulations of sound propagation using these effective medium models have been recently shown to be well-posed [30]. If one assumes that $\Gamma_C < 2\omega_{*C}$ and $\Gamma_\rho < 2\omega_{*\rho}$, these models are equivalent to a pair of complex-conjugate poles. For example, for the effective compressibility:

$$C_e(\omega) = \frac{\phi}{\rho_0 c_0^2} + \frac{\mathrm{j}C_C}{\alpha_C + \mathrm{j}\beta_C + \mathrm{j}\omega} + \frac{-\mathrm{j}C_C}{\alpha_C - \mathrm{j}\beta_C + \mathrm{j}\omega},$$
$$\alpha_C = -\frac{\Gamma_C}{2}, \quad \beta_C = \frac{\sqrt{-\Gamma_C^2 + 4\omega_{*C}^2}}{2}, \quad C_C = \frac{\phi}{\rho_0 c_0^2} \frac{F_C \omega_{*C}^2}{\sqrt{-\Gamma_C^2 + 4\omega_{*C}^2}}.$$

For simplicity, only a resonance of the effective compressibility at 1000 Hz has been considered in this study, leading to two kinds of behavior: a double-positive material (DP), where $\rho_e > 0$ and $C_e > 0$, and a band gap (BG), where $\rho_e > 0$ and $C_e < 0$. Within the BG, the sound speed (real component) vanishes and thus sound propagation through the material is theoretically suppressed. As a baseline case we have set $F_C = 2$, $\Gamma_C = 300$ and $\phi = 1$. Fig. 5a shows the effective density and the effective compressibility. Three frequency bands can be identified depending on the relative signs of ρ_e and C_e: a DP region for $f < 1000$ Hz, a BG in 1000 Hz$< f <$ 1460 Hz, and a DP for $f > 1460$ Hz. Fig. 5b shows the real part of the sound speed in the metamaterial. It is close to zero in the band gap, and undergoes a sudden increase in the BG-DP boundary. Note that only in the low- and high-frequency limits the sound speed in the material approaches the sound speed of air.

4.3. Perforated plates

There exist a number of models of $Z_{sh}(\omega)$ for perforated plates and screens. Here the classical model of Maa [31,52] has been used, but more refined models can be applied if necessary. In this study two perforated plates have been considered, corresponding to largely different geometries. PS1 is a very thin plate with large circular perforations and large porosity. On the other hand, PS2 is a thick plate with very small holes and low porosity. Their geometrical values are shown in Table 2. Their impedance is shown in Fig. 6a,b. It appears that two real poles are sufficient to describe accurately the functions K_{sh1} and K_{sh2} in a large frequency range. Fig. 6c,d show the fit of K_{sh1} corresponding to PS1 and PS2 with two real poles.

5. 1D test case: validation against analytical solution

Results of a 1D test case are here presented with the aim of validating the methodology proposed in section 3 for extended-reacting liners with a dissipative interface. In addition, it is checked that the global order of accuracy of the nu-

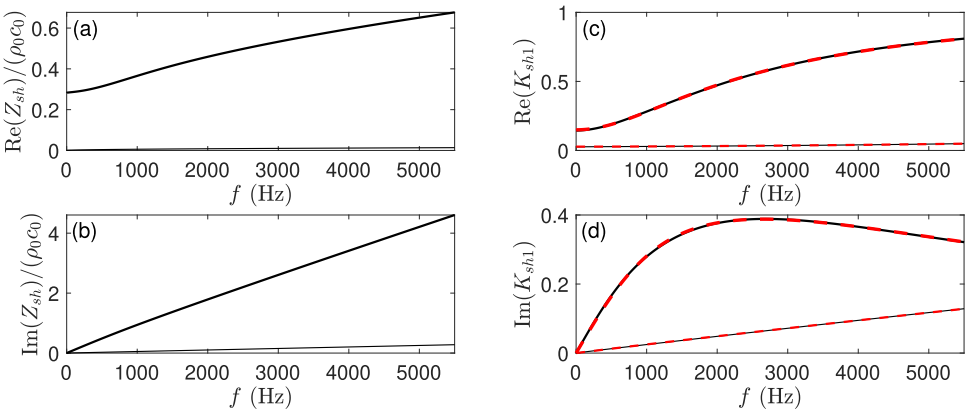

Fig. 6. (a,b) Real and imaginary components of the impedance of the perforated sheets PS1 (——) and PS2 (——); (b,c) real and imaginary components of the auxiliary interface function K_{sh1} for PS1 (——) and PS2 (——), and their approximations with 2 real poles (- - - and - - -, respectively).

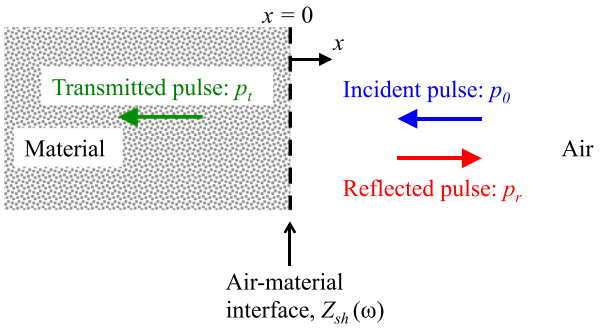

Fig. 7. Sketch of the 1D test case configuration.

merical solver is not degraded, and the different sources of error are highlighted. The codes used to produce these results are available in the supplementary material.

The 1D test case configuration is shown in Fig. 7. A plane wave pulse incident on an interface between air and a sound-absorbing material is partly reflected and partly transmitted. The interface is located at $x = 0$, the semi-infinite medium $x > 0$ and $x < 0$ corresponds to the air and to the material, respectively. Note that the interface can be dissipative and induce a pressure jump. The analytical solution to this problem is detailed in Appendix B. The same numerical schemes and selective filters of the 2D configuration are used, except for the second-order non-centered selective filters that are not employed in this section. The grid size is uniform everywhere in the domain, with a reference value of $\mathrm{d}x = 0.005$ m. The time step is set so that the CFL number, defined by $\mathrm{CFL} = c_0 \mathrm{d}t/\mathrm{d}x$, is equal to one, which yields a reference time step $\mathrm{d}t = 1.47 \times 10^{-5}$ s. The strength of the selective filters is set to 0.2 for all the simulations. The FDTD algorithm is advanced in time starting from the initial conditions:

$$p(x > 0, t = 0) = p_0(x - x_s), \qquad p(x < 0, t = 0) = 0$$
$$v(x > 0, t = 0) = -p_0(x - x_s)/(\rho_0 c_0), \qquad v(x < 0, t = 0) = 0$$

where p_0 is a Mexican hat pulse

$$p_0(x) = \left(1 - \left[\frac{x}{B}\right]^2\right) \exp\left(-\left[\frac{x}{\sqrt{2}B}\right]^2\right)$$

of width $B = 0.015$ m and centered initially at $x_s = 1$ m. With this value of B, the incident pulse has frequency contents up to approximately 15 kHz. The auxiliary functions are all initialized to zero.

Fig. 8a shows three successive snapshots of the pressure field obtained for a semi-infinite layer of polyurethane foam covered by the perforated plate PS2. The pulse at t_1 is the incident pulse. At t_2 the incident pulse impinges on the perforated sheet. Note the pressure jump at the interface due to the perforated sheet. Finally, at t_f the pulse transmitted through the perforated sheet and propagating in the foam and the pulse reflected at the interface are clearly identified. Fig. 8b shows the associated error distributions, determined with the analytical solution. Note that the error is small both for the reflected and transmitted pulse.

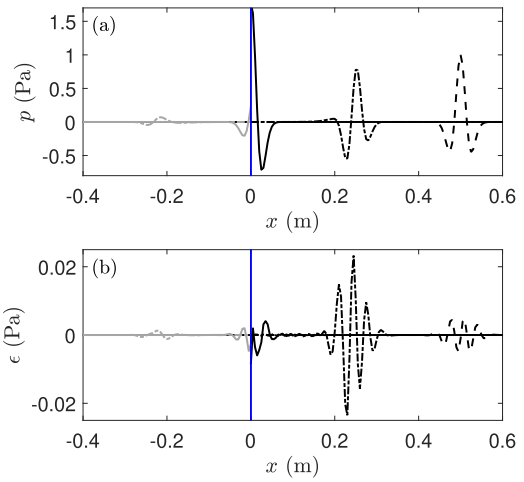

Fig. 8. (a) Pressure field from FDTD in the air and in the polyurethane foam covered with PS2, at $t_1 = 1.5$ ms (initial pulse, - - -), $t_2 = 2.9$ ms (during impingement on the impedance wall, ——— and ———) and $t_f = 3.7$ ms (transmitted and reflected pulses, - · - · - and - · - · -); (b) error of the pressure field from FDTD.

In order to analyze more precisely the error induced by the treatment of the material and of the interface, a convergence study as the timestep dt is reduced from its reference value is now performed. The errors are determined separately for the air domain ($x > 0$) and the material domain ($x < 0$), with the aim of characterizing individually the reflection and the transmission. The following measure of the global error is considered:

$$\epsilon_{\text{tot}} = \sqrt{\frac{\int |p(x,t_f) - p_{\text{ana}}(x,t_f)|^2 \,\mathrm{d}x}{\int |p_{\text{ana}}(x,t_f)|^2 \,\mathrm{d}x}}, \tag{19}$$

where the integral is performed at a time $t_f = 3.7$ ms over each considered domain. The errors in the air and material domains are hereafter indicated by the superscript ^{a} and ^{m}, respectively. The error curves are obtained at a constant CFL $= c_0\,\mathrm{d}t/\mathrm{d}x$ of 1, which implies that the mesh size varies linearly with the time step.

In the general case, the numerical solution from FDTD has two sources of error, namely the modeling error induced by the pole truncation of ρ_e and C_e and of K_{sh1} and K_{sh2}, and the numerical error, due to the discretization:

$$\underbrace{p - p_{\text{ana}}}_{\text{total}} = \underbrace{p - p_{\text{ana, mod}}}_{\text{numerical}} + \underbrace{p_{\text{ana, mod}} - p_{\text{ana}}}_{\text{modeling}},$$

where p is the numerical solution, p_{ana} is the analytical solution built from the exact values of ρ_e, C_e and Z_{sh}, and $p_{\text{ana, mod}}$ is the analytical solution built from the truncated partial fraction expansions of ρ_e, C_e, K_{sh1} and K_{sh2}. Note that if the medium on both sides of the interface corresponds to air the error associated to the truncation of ρ_e and C_e is zero, and in the case of a free or constant resistance interface the interface conditions are exact. In order to characterize these two error contributions, we define the numerical error ϵ_{num} and the modeling error ϵ_{mod} by:

$$\epsilon_{\text{num}} = \sqrt{\frac{\int |p(x,t_f) - p_{\text{ana,mod}}(x,t_f)|^2 \mathrm{d}x}{\int |p_{\text{ana}}(x,t_f)|^2 \mathrm{d}x}}, \qquad \epsilon_{\text{mod}} = \sqrt{\frac{\int |p_{\text{ana, mod}}(x,t_f) - p_{\text{ana}}(x,t_f)|^2 \mathrm{d}x}{\int |p_{\text{ana}}(x,t_f)|^2 \mathrm{d}x}},$$

where the full analytical solution is always used as the normalization factor for consistency.

Fig. 9a illustrates the convergence of the error for the reflected wave with the time step for the polyurethane foam covered with PS2. For large timesteps, the total error is mostly due to the numerical error. The decrease of the error with the timestep is thus depending on the numerical schemes and the numerical order of the FDTD algorithm emerges. For smaller timesteps, the error converges to the modeling error due to the truncation of ρ_e and C_e and/or the interface functions K_{sh1} and K_{sh2}, and ceases to depend on the timestep. The corresponding convergence of the error for the transmitted pulse is shown in Fig. 9b. In this case, except for the largest timesteps, the total error is entirely due to the modeling error.

Fig. 10 depicts the total error (ϵ_{tot}) curves and the modeling error (ϵ_{mod}) corresponding to an increasing number of real poles used to describe the effective density and effective compressibility of the aluminum foam without any covering sheet. The errors determined for the reflected and transmitted waves show a saturation of the total error at small timesteps, due to the pole truncation error. The pole truncation error decreases fast until 4 real poles, while the error for 5 poles is only marginally lower than with 4 poles, indicating a certain saturation. Note that such saturation was not observed in the error of ρ_e and C_e (see Fig. 3). At the largest timestep, the total error for the reflected wave is dominated by the numerical error, and is approximately independent of the number of poles retained.

Similarly, Fig. 11 shows the total error curves and the modeling error curves associated to the pole truncation of K_{sh1} and K_{sh2} (ϵ_{mod}), for two semi-infinite layers of air separated by the perforated plate PS2 using 2, 4 and 6 real poles to describe

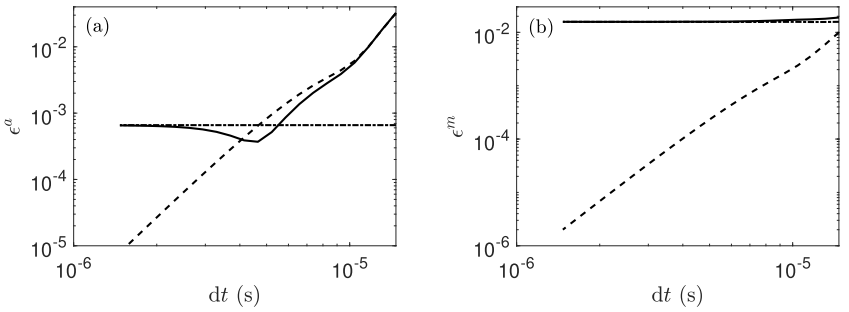

Fig. 9. ϵ_{tot} (——), ϵ_{num} (– – –) and ϵ_{mod} (–·–·–) corresponding to the polyurethane foam covered with PS2 determined (a) for the reflected wave in the air and (b) for the transmitted wave in the foam.

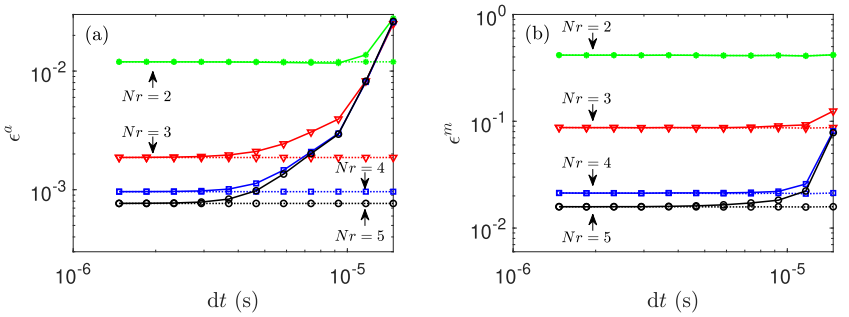

Fig. 10. ϵ_{tot} and ϵ_{mod} corresponding to the aluminum foam without a perforated sheet for 2 real poles (—✳—, ··✳··), 3 real poles (—▽—, ··▽··), 4 real poles (—□—, ··□··) and 5 real poles (—○—, ··○··) of ρ_e and C_e, determined (a) for the reflected wave in the air and (b) for the transmitted wave in the foam.

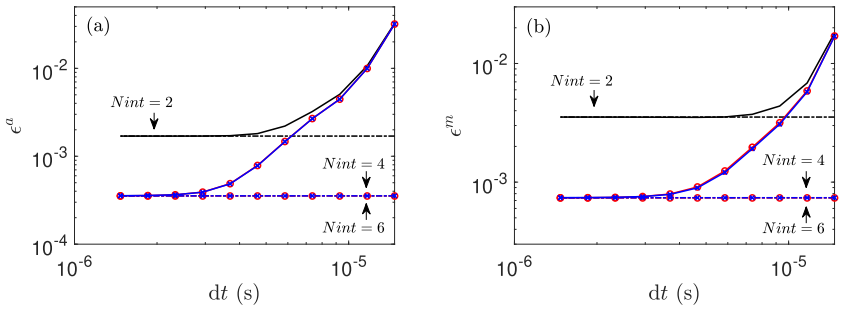

Fig. 11. ϵ_{tot} and ϵ_{mod} for two semi-infinite layers of air separated by the perforated sheet PS2 using 2 interface poles (—— and –·–·–), 4 interface poles (—○— and – ○ ·-) and 6 interface poles (—×— and –·×·–) determined (a) for the reflected wave and (b) for the transmitted wave.

K_{sh1} and K_{sh2}. The shape of the curves is similar to that in Fig. 10, for both the reflected and transmitted waves. At small timesteps the decrease of the total error saturates due to the interface pole truncation error. Note that increasing from 4 to 6 poles does not lead to a significant decrease of the pole truncation error. At large timesteps the total error is dominated by the numerical error and appears to be independent of the number of poles retained.

Fig. 12 shows the numerical error curves for several simulations associated to different configurations: a semi-infinite medium corresponding to a porous medium or by air and with or without covering sheet, which can be a purely resistive screen or a perforated plate. All these curves, both for the reflected and transmitted waves, show the same variations with the timestep. In particular, at small timesteps the numerical error decreases as dt^4, which corresponds to the lowest order of all the numerical schemes employed in this test case (Runge-Kutta, finite-difference and selective filters).[1] Overall, this convergence study shows that the numerical treatment of the porous medium and of the interface does not degrade the order of accuracy of the solver. Therefore, the methodology proposed here is in particular well-suited for high-order solvers.

In this section the FDTD code has been validated against the analytical solution in a 1D configuration. The role of the number of poles retained for the effective density and compressibility and for the broadband interface condition in the

[1] It should be noted that the use of the second-order non-centered filters near the interface would lead to a reduction of the accuracy order from fourth order to second order.

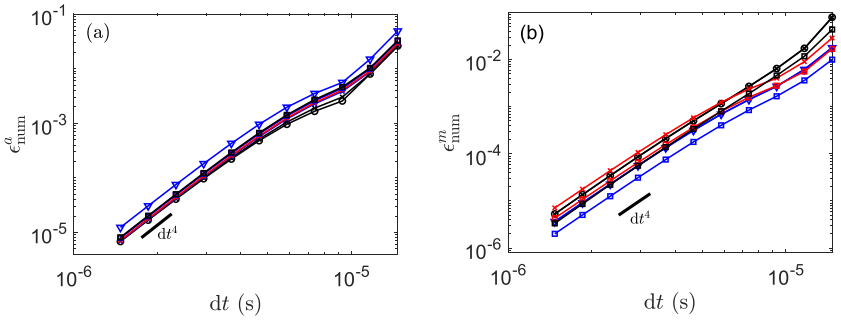

Fig. 12. $\epsilon_{\rm num}$ determined (a) for the reflected wave and (b) for the transmitted wave and for various configurations: a semi-infinite layer of air (——), aluminum (——) or polyurethane (——) without covering (○) or covered with a resistive sheet with $R_{sh} = 0.5\rho_0 c_0$ (×) or with the perforated plate PS1 (▽) or PS2 (□).

total numerical error has been exposed. Finally, the numerical order of the algorithm has been shown to be recovered, independently of the liner material or the perforated sheet, as long as a sufficient number of poles is retained.

6. 2D lined duct

The solver is applied now to a 2D duct with a side cavity filled with the liner material (see Fig. 1). Cavities ranging from a short and deep cavity with $L_m/H_m = 0.25$, to a long and shallow cavity with $L_m/H_m = 10$, have been considered. While the former cavities are expected to be approximately locally-reacting (at moderate frequencies), the latter is a case of marked extended-reacting behaviour, as will be shown in Sec. 6.4. The forcing consists of a plane pulse located either upstream or downstream of the treated section:

$$Q(x,t) = \lambda(t)\frac{x - x_S}{x_c}\exp\left(-\left[\frac{(x - x_S)}{\sqrt{2}x_c}\right]^2\right), \tag{20}$$

$$\lambda(t) = \frac{t - t_S}{t_c}\exp\left(-\left[\frac{(t - t_S)}{\sqrt{2}t_c}\right]^2\right), \tag{21}$$

where $x_c = 8\,\mathrm{d}x$, $t_S = 5 \cdot 10^{-4}$ s and $t_c = 10^{-4}$ s. These values have been chosen to assure that the vast majority of the signal energy is below the cutoff frequency of the rigid duct, and also that the temporal pulse is entirely located at $t > 0$.

6.1. Scattering matrix

For frequencies lower than the rigid duct cutoff frequency, and assuming a uniform mean flow, the acoustic field in the upstream (1) and downstream (2) rigid sections is the sum of a right-propagating (+) and a left-propagating (-) convected plane waves:

$$\hat{p}_1(x,\omega) = A_1^+\exp(-\mathrm{j}k_0^+x) + A_1^-\exp(\mathrm{j}k_0^-x),$$
$$\hat{p}_2(x,\omega) = A_2^+\exp(-\mathrm{j}k_0^+x) + A_2^-\exp(\mathrm{j}k_0^-x),$$
$$k_0^+ = \frac{\omega}{c_0(1+M)}, \quad k_0^- = \frac{\omega}{c_0(1-M)}$$

where A_1^+, A_1^- are the complex amplitudes in the upstream rigid section, and A_2^+, A_2^- are the complex amplitudes in the downstream rigid section. The response of the liner to incoming plane waves can be defined in terms of a scattering matrix:

$$\begin{pmatrix} A_2^+ \\ A_1^- \end{pmatrix} = \begin{pmatrix} T^+ & R^- \\ R^+ & T^- \end{pmatrix}\begin{pmatrix} A_1^+ \\ A_2^- \end{pmatrix},$$

where T^+, T^- are the transmission coefficients for an upstream source and a downstream source, respectively, and R^+, R^- are the corresponding reflection coefficients. The transmission and reflection coefficients are complex functions of frequency. If $M = 0$ the system is symmetric and thus $T^+ = T^- = T$ and $R^+ = R^- = R$. In this case T and R are determined by a single simulation. The presence of a mean flow breaks the +/- symmetry, and two simulations corresponding to two different configurations are needed to determine the four scattering coefficients. The transmission and reflection coefficients have been computed here using the two-source method [53,54], which is widely used in experiments. Two sensors upstream and two sensors downstream have been used to compute the scattering matrix. The distance between the sensors of each

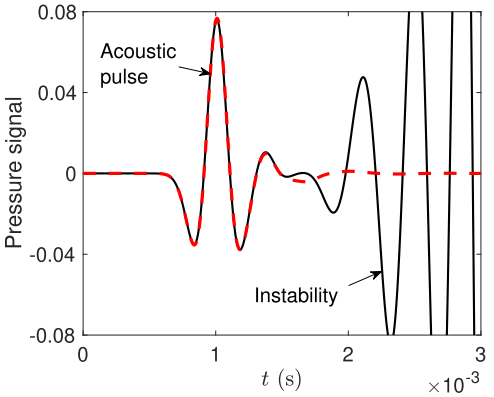

Fig. 13. Comparison of the pressure signal on the opposite wall of the liner, at the center of the lined section, for the short cavity filled with the polyurethane foam, without the GTS method (——) and with the GTS method (- - -).

pair is slightly smaller than half the wavelength of the plane waves traveling upstream (the most restrictive case), i.e. $c_0(1-M)/(2f_{\max})$, where $f_{\max}$ is the largest frequency considered. This moves the first $\lambda/2$-indeterminacy to a frequency slightly larger than $f_{\max}$. The details of the calculation of the scattering matrix from the sensor signals are included in Appendix C.

6.2. Gradient term suppression method (GTS)

The LEE equations on a mean shear flow over a lined wall can sustain hydrodynamic instabilities, which are excited by incoming sound waves. These unstable modes can be physical [55,56] or generated by the discretization of the continuous equations [57]. Time-domain simulations are especially susceptible to instabilities because they are broadband in nature and so any unstable mode will be excited. Indeed, from the FDTD simulations it appears that the hydrodynamic instability is ubiquitous in the extended-reacting liners considered here, as soon as the Mach number exceeds about 0.1. The instability appears to be stronger on an extended-reacting liner than on the equivalent locally-reacting liner, for both short and long cavities. Though not presented here, the addition of a smooth-wall turbulent viscosity profile has also been tested, and it is not enough to transform the instability from absolute to convective, which has been shown to be the case for certain locally-reacting liners [58].

In this study we have used the gradient term suppression method (GTS) [59] to eradicate all instabilities. This method is simple and robust, and is close to competing methods in the case of jets [60]. It was also shown to be efficient to suppress the hydrodynamic instability generated over a locally-reacting liner [61]. The main drawback is that the GTS method also modifies the acoustic field. Its impact on the acoustic duct modes was assessed in [61]. The GTS method consists of eliminating the mean flow gradient term in the x-momentum equation ($\nu \mathrm{d}U_0/\mathrm{d}y$) responsible for the acoustic-vorticity coupling in the LEE equations [59]. Fig. 13 shows the pressure signal sampled on the opposite wall of the liner, at the liner central section, for the short cavity filled with the polyurethane foam, with and without GTS. Note the good match of the initial acoustic pulse and the suppression of the oscillations due to the instability by GTS.

6.3. Validation against experimental results

The experimental results of Aurégan and Singh [62] with a rigid-frame, Nickel-Chrome porous liner ($\phi = 0.99, \alpha_\infty = 1.17, \Lambda = 1.0 \cdot 10^{-4}$ m, $\Lambda' = 2.4 \cdot 10^{-4}$ m) have been used to validate the FDTD code. In this case the duct height was 0.015 m, the liner length 0.2 m, and the liner depth 0.025 m. The comparison for $M = 0$ is shown in Fig. 14a. The predictions of both $|T|$ and $|R|$ are excellent. The same results in the case of $M = 0.2$ are shown in Figs. 14c,d. The trends of $|T^+|$ and $|R^+|$ are remarkably accurate overall. On the other hand, while the trends of $|T^-|$ and $|R^-|$ are well predicted, their value is overestimated by about 10-20%. The measured pattern of $|T^+|$ reveals oscillations in the range 500-1500 Hz that are not captured by the temporal simulations. These are related to the hydrodynamic instability wave that grows along the lined wall. The frequency of the peaks and troughs is determined by the relative phase lag of the acoustic wave and the instability wave at the liner end section [56,62]. The GTS method suppresses completely the instability wave and therefore the oscillations are absent from the simulations.

Given the remarkable accuracy of the predicted scattering coefficients for $M = 0$, it is likely that the differences observed at $M = 0.2$ are not due to an inaccuracy of the JCA parameters of the metallic foam, but due to an actual mis-modeling of either the mean flow profile, the presence of a mean flow in the material [56], or the use of GTS. However, the present results show that a good approximation can be achieved with the current simplified model.

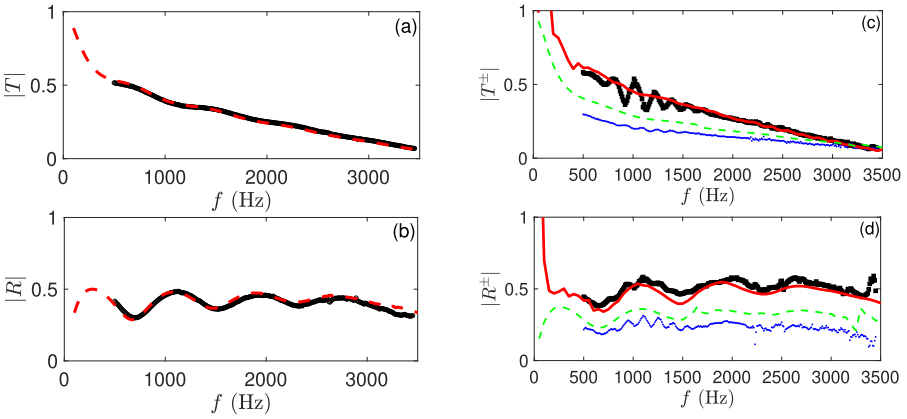

Fig. 14. (a,b) FDTD prediction of $|T|, |R|$ (▪▪▪) and measurement (○), for $M = 0$; (c,d) FDTD prediction of $|T^+|, |R^+|$ (——), and $|T^-|, |R^-|$ (▪▪▪), and measurement of $|T^+|, |R^+|$ (□) and $|T^-|, |R^-|$ (▪), for $M = 0.2$ and a liner cavity with $L_m = 200$ mm and $H_m = 25$ mm.

6.4. Extended-reacting behavior

In this section the approximation of extended-reacting liners by a surface impedance is addressed. While in the 1D configuration the layer of sound-absorbing material is always equivalent to its surface impedance, this is not true in general in 2D or 3D configurations. In this case a locally-reacting behavior can only be expected when sound waves inside the liner cavity propagate in the wall-normal direction, i.e. when only the plane wave mode propagates inside the liner cavity. A first condition is that the acoustic wavelength in the main duct is much larger than the cavity length, which is equivalent to a low-frequency condition, $f \ll c_0/L_m$. This assures that the most excited mode in the cavity is the plane wave mode. Another condition is that the cavity depth is much larger than the acoustic wavelength inside the cavity. This ensures that the least attenuated mode, i.e. the plane wave mode, will dominate the acoustic field. While the first condition is purely geometric, the second one depends also on the material. Note that a mean flow in the duct changes the wavelength of the acoustic waves: the wavelength of downstream-propagating waves increases, and the wavelength of upstream-propagating waves decreases. An impact of the flow on the validity of the locally-reacting approximation is then expected, which increases with the Mach number.

As a showcase of locally-reacting and extended-reacting behavior we have considered two cavities: a short and deep one ($L_m = 10$ mm and $H_m = 40$ mm) and another one which is long and shallow ($L_m = 100$ mm and $H_m = 10$ mm). While the short cavity fulfills the geometric condition for a locally-reacting behavior in the considered frequency range, the long cavity does not, except at very low frequencies, and therefore a marked extended-reacting behavior can be expected independently of the liner material. The duct height is set to $H = 0.02$ m, and the length of the duct section with a uniform grid is 0.392 m (limited by the beginning of the sponge zones). The central section of the cavity is fixed at the central section of the duct. The upstream and downstream sources are located at 0.046 m from the upstream and downstream sponge zones, respectively. The inner pressure sensors are fixed at 0.05 m from the long cavity and at 0.1 m from the short cavity. The outer sensors are separated by 0.05 m from the sources. It has been checked that changes of these distances don't affect significantly the scattering matrix.

A modified version of the FDTD solver has been used to compute the acoustic field in the case of a locally-reacting liner, with a surface impedance determined by:

$$Z_s(\omega) = -\mathrm{j} Z_e(\omega) \cot(k_e(\omega) H_m) + Z_{sh}(\omega), \tag{22}$$

where the material characteristic impedance, Z_e, and wavenumber, k_e, are defined as

$$Z_e(\omega) = \sqrt{\frac{\rho_e(\omega)}{C_e(\omega)}}, \quad k_e(\omega) = \omega \sqrt{\rho_e(\omega) C_e(\omega)}.$$

The no-flow impedance boundary condition is used because the mean flow velocity is zero on the lined wall. The locally-reacting solver uses the same numerical schemes than the extended-reacting FDTD solver, and the ADE method is used to transform the impedance boundary condition to the time-domain [37].

Simulations are performed for the two porous materials and for the metamaterial, whose effective properties are shown in Figs. 4 and 5a. As an example, the computational cost of the approach is indicated for the aluminum foam. The effective density and compressibility are approximated using 5 poles. There are thus 18 variables for the material domain: p, u, v and 15 auxiliary functions ($\phi^x_{\rho k}$, $\phi^y_{\rho k}$ and ϕ_{Ck} for $1 \leq k \leq 5$), while there are three variables in the air domain: p, u and v. There are 92500 points in the air domain and 9100 points in the material domain for the long cavity and 3800 points for the short cavity. Compared to the simulation with an impedance boundary condition, this leads to an increase of memory

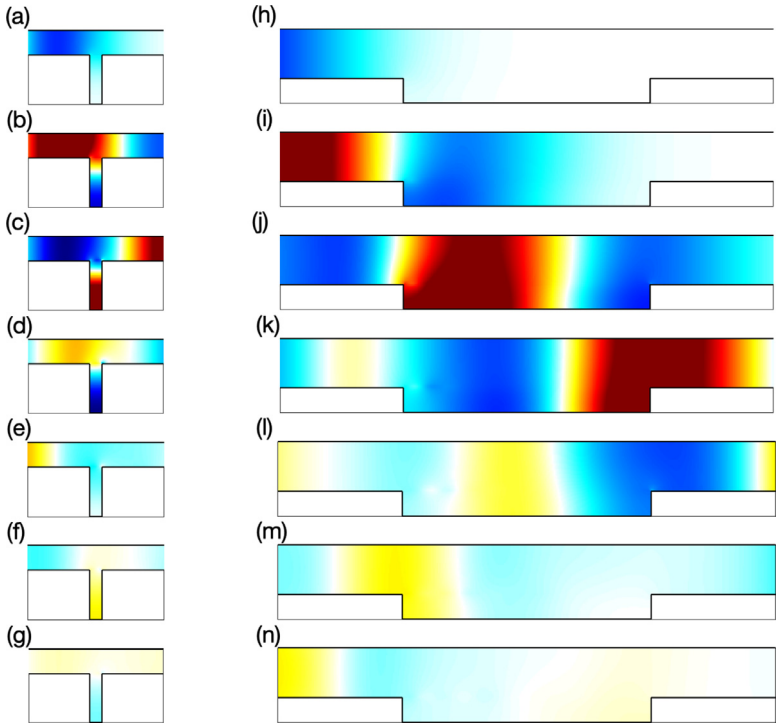

Fig. 15. Successive snapshots of the pressure field for the short cavity (a-g) and the long cavity (h-n), both filled with the aluminum foam, at $M = 0.3$ and with the upstream source; short cavity: starting from $t = 9.6 \cdot 10^{-5}$ s and sampled every $9.6 \cdot 10^{-6}$ s; long cavity: starting from $t = 7.68 \cdot 10^{-5}$ s and sampled every $1.92 \cdot 10^{-5}$ s.

usage by 60 % and 25 % for the long and short cavity, respectively, and to a corresponding increase of CPU time by 80 % and by 50 %.

6.4.1. Porous material

Fig. 15a-g display the evolution of the pressure field in the duct section lined with the short cavity filled with the aluminum foam, with a mean flow at $M = 0.3$ and the acoustic source placed upstream (flow goes from left to right). It is appreciated that the plane wave mode dominates the pressure field both in the duct and within the cavity. The latter indicates that substituting the cavity by a locally-reacting liner seems to be appropriate in this case. Fig. 15h-n show the analogous plots for the long cavity. Note that, while the pressure is continuous at the air-material interface, the y-gradient of the pressure is discontinuous. In this case the near-plane mode (which coincides with the least attenuated mode) of the lined section seems to be dominant along the lined section.

Fig. 16a,b,c,d compare the transmission (a,c) and reflection (b,d) coefficients against the predictions using a locally-reacting approximation, corresponding to the two porous materials for the short and deep cavity (a,b) and the long and narrow cavity (c,d). In the locally-reacting approximation the impedance of the liner is calculated using Eq. (22). While the locally-reacting approximation is accurate for the short cavity for all materials tested, it fails for the long cavity, as expected. In short cavities it is generally observed that the approximation is worse around the $\lambda/4$-resonances of the cavity, and that in this situation the approximation is better for the high resistivity porous materials than for low resistivity materials. When approaching these cavity resonances the waves propagating inside the cavity have a larger impact on the acoustic field in the main duct, and thus the locally-reacting approximation leads to higher relative errors of the transmission and reflection coefficients. Higher resistivity materials lead to higher decay rates of the plane wave mode inside the cavity, diminishing the strength of the cavity resonance and thus diminishing the relative error of the locally-reacting approximation. Fig. 17a,b show the transmission and reflection coefficients of the short cavity filled with aluminum foam for $M = 0.3$. The locally-reacting approximation is also excellent in this case, with slightly lower accuracy in the case of the downstream source, which can be explained by the smaller wavelength of the plane waves traveling upstream.

It is interesting to examine the surface impedance along the lined wall from the extended-reacting liner simulations. It is obtained from the Fourier transforms of the pressure and wall-normal velocity at the interface:

$$Z_s(x, \omega) = -\frac{\hat{p}(x, \omega)}{\hat{v}(x, \omega)}. \tag{23}$$

In the case of an *ideal* locally-reacting liner, the surface impedance should be constant along the liner, independent from the source location, independent from the flow, and equal to the value provided by Eq. (22). The surface impedance of

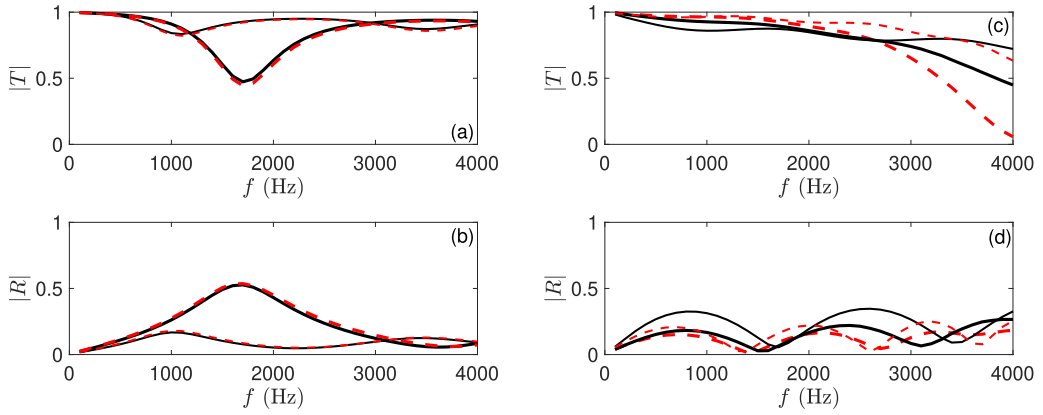

Fig. 16. FDTD prediction of $|T|, |R|$ for the extended-reacting polyurethane foam liner (——), extended-reacting aluminum foam liner (——), locally-reacting polyurethane foam liner (- - -), and the locally-reacting aluminum foam liner (- - -), corresponding to the short cavity (a,b) and the long cavity (c,d) at $M = 0$.

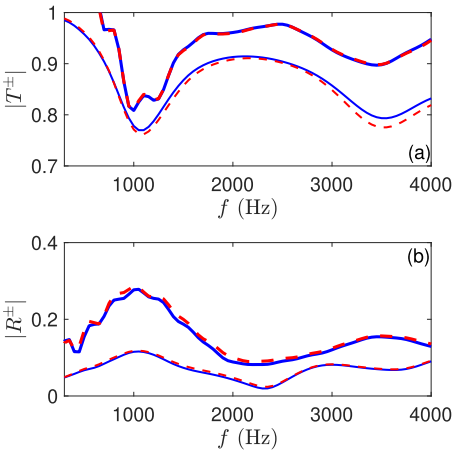

Fig. 17. FDTD prediction of $|T^+|, |R^+|$ corresponding to the extended-reacting case (——) and the locally-reacting case (- - -), and prediction of $|T^-|, |R^-|$ corresponding to the extended-reacting case (——) and the locally-reacting case (- - -), for the short cavity filled with aluminum foam at $M = 0.3$.

the short cavity filled with aluminum foam at $M = 0$ and $M = 0.3$, for an upstream source and a downstream source, are plotted in Fig. 18a,b (1000 Hz) and Fig. 18c,d (4000 Hz). Note that the surface impedance obtained from the extended-reacting configuration suffers significant changes along the liner, even without flow. As expected, the curves corresponding to $M = 0$ are symmetric with respect to the center of the liner. The mean flow breaks this symmetry. The mean value of surface impedance from the extended-reacting configuration is, however, not far from the locally-reacting impedance, the extended-reacting effect being approximately antisymmetric with respect to the center of the liner. At both frequencies, and especially at 1000 Hz, the cavity is approximately equivalent to a point-like impedance, with the dominant contribution coming from the plane wave inside the cavity. In this situation, the effect of higher-order evanescent modes inside the cavity may be important in the immediate vicinity of the air-material interface, but become negligible away from it. It is nevertheless surprising that the plane wave scattering coefficients from the extended-reacting and locally-reacting liners are so close for the short cavity, given these differences in surface impedance between both cases, and between upstream and downstream sources.

6.4.2. Locally-resonant metamaterial

Fig. 19a,b,c,d compare the transmission (a,c) and reflection (b,d) coefficients against the predictions using a locally-reacting approximation, corresponding to the short cavity (a,b) and the long cavity (c,d), filled with a metamaterial based on a local resonance of the effective compressibility at 1000 Hz. As for the porous materials, the locally-reacting approximation in the short cavity is excellent in all the frequency range considered. In the case of the long cavity the agreement is overall worse, as expected. Fig. 20a,b show the absolute value of the transmission coefficient for the short cavity (a) and the long cavity (b) at $M = 0.3$, corresponding to the extended-reacting and the locally-reacting cases. Interestingly, the locally-reacting approximation for the short cavity is overall worse than without flow. With the upstream source the prediction from the locally-reacting approximation is reasonable for all frequencies. But for the downstream source important differ-

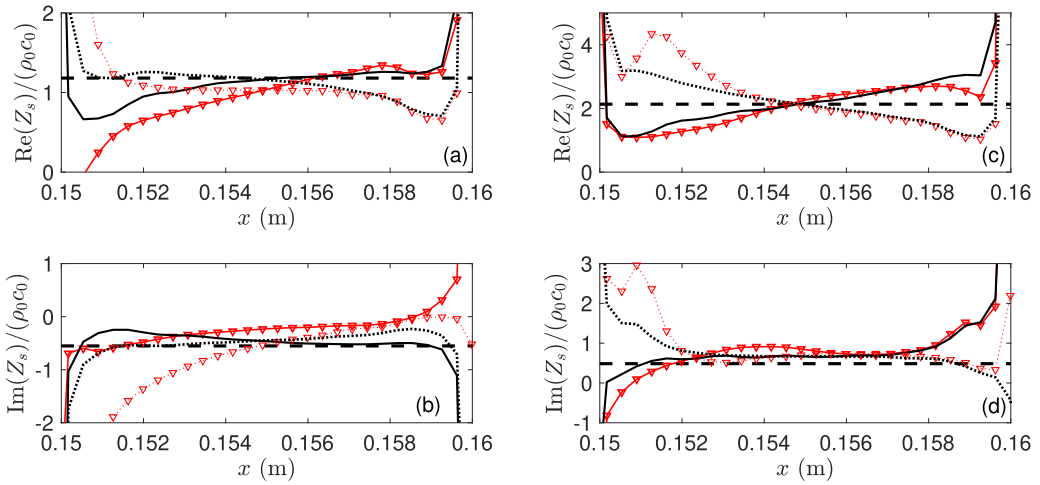

Fig. 18. Surface impedance along the short cavity filled with aluminum foam, at (a,b) 1000 Hz and (c,d) 4000 Hz, for the extended-reacting liner with an upstream source at $M = 0$ (——), $M = 0.3$ (—▽—), the extended-reacting liner with a downstream source at $M = 0$ (▪▪▪▪), $M = 0.3$ (··▽··), and the locally-reacting approximation (▪ ▪ ▪).

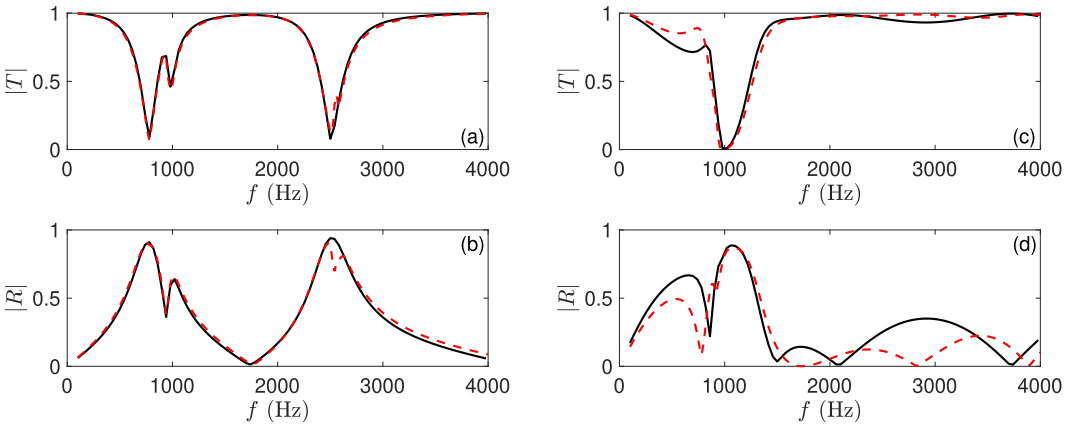

Fig. 19. Transmission and reflection coefficients for the extended-reacting case (——) and the locally-reacting approximation (▪ ▪ ▪), of the short cavity (a,b) and the long cavity (c,d) filled with a metamaterial with a local resonance of the effective compressibility at 1000 Hz, $F_C = 2$ and $\Gamma_C = 300$, at $M = 0$.

ences are observed, notably around the cavity resonances at 750 Hz and 2500 Hz. This is attributed to the effect of flow on the wavelength of incoming waves: in the case of a downstream source the wavelength of the incoming plane waves is significantly lower than without flow (about a 30% lower), limiting the validity of the long wavelength assumption.

Concerning the long cavity, it is observed that below 1000 Hz the locally-reacting approximation is not accurate for both upstream and downstream sources. Similarly to the case without flow, from about 1000 Hz to about 1500 Hz the transmission coefficient from the locally-reacting approximation approaches the transmission coefficient of the extended-reacting liner.

Notice that in the range 1000 Hz $< f <$ 1500 Hz the locally-reacting approximation of the long cavity is reasonably accurate for both $M = 0$ and $M = 0.3$. This frequency band coincides with the frequency band where the sound speed inside the material cavity is close to zero (see Fig. 5b). For long cavities, it is the least attenuated mode of the lined section that dominates the acoustic field. We have computed the eigenmodes of the duct lined with a metamaterial layer of depth $H_m = 0.01$ m for both the extended-reacting case and the locally-reacting approximation, for $M = 0$. We have used a second-order finite-difference discretization in the wall-normal direction. In the extended-reacting case, the continuity of pressure and wall-normal velocity has been imposed at the air-material interface. In terms of pressure the interface condition is:

$$\hat{p}_a = \hat{p}_m,$$
$$\frac{1}{\rho_0}\frac{\partial \hat{p}_a}{\partial y} = \frac{1}{\rho_e(\omega)}\frac{\partial \hat{p}_m}{\partial y},$$

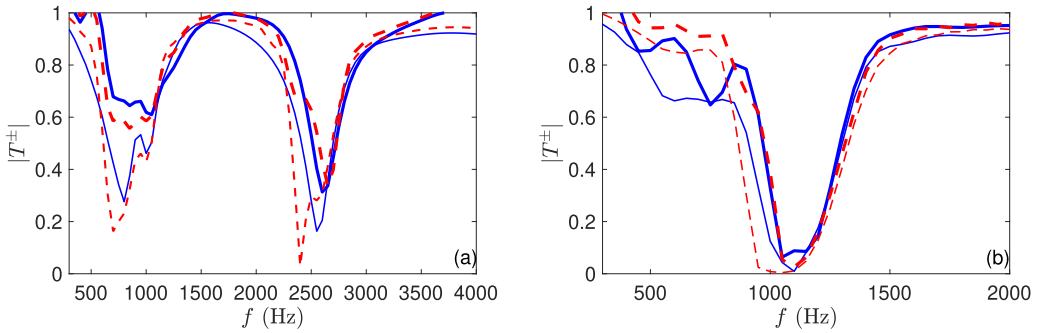

Fig. 20. $|T^{+}|$ for the extended-reacting case (——) and the locally-reacting approximation (——), $|T^{-}|$ for the extended-reacting case (- - -) and the locally-reacting approximation (- - -), for the metamaterial in the short cavity (a) and the long cavity (b), at $M = 0.3$.

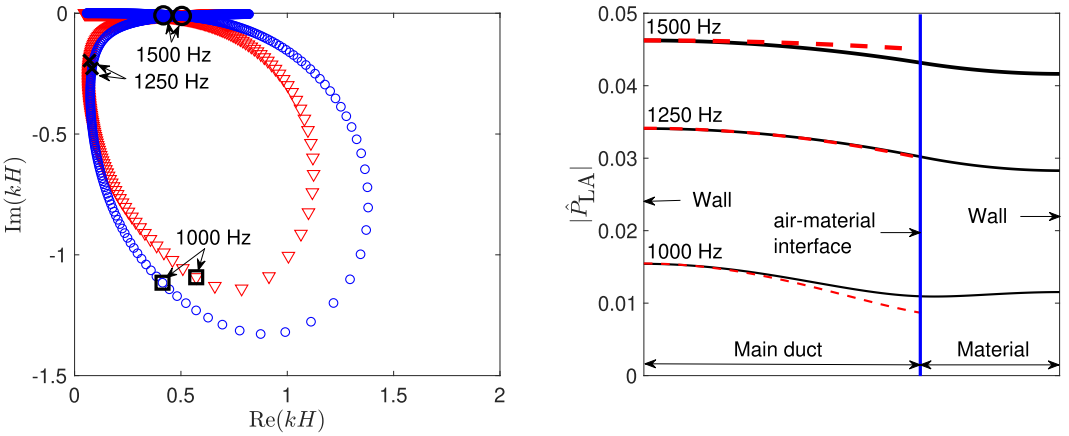

Fig. 21. (a) Wavenumbers of the least attenuated mode for the long cavity ($H_m = 0.01$ m) filled with the metamaterial, corresponding to the extended-reacting case (▽) and the locally-reacting approximation (○); (b) mode shapes (amplitude) of the least attenuated mode for the extended-reacting liner at 1000 Hz (——), 1250 Hz (——) and 1500 Hz (——), and amplitude of the least attenuated mode for the locally-reacting liner at 1000 Hz (- - -), 1250 Hz (- - -) and 1500 Hz (- - -). The metamaterial has a local resonance of the compressibility at 1000 Hz, with parameters $F_C = 1.7$ and $\Gamma_C = 300$.

In the locally-reacting case the impedance obtained from Eq. (22) is imposed at the boundary through:

$$\frac{\partial \hat{p}_a}{\partial y} = -\frac{\rho_0 \omega}{\mathrm{j} Z_s(\omega)} \hat{p}_a.$$

Fig. 21a shows the wavenumbers of the least attenuated mode for frequencies in the range 100 Hz $< f <$ 2000 Hz. Fig. 21b shows the amplitude of the least attenuated mode at three different frequencies, for the extended-reacting and locally-reacting cases. In the frequency range 1000 Hz $< f <$ 1500 Hz the wavenumbers and the mode shapes of the extended-reacting and locally-reacting cases are similar, explaining the match in the transmission and reflection coefficients.

6.5. Impact of the mean flow on the acoustic performance

In this section we evaluate the impact of the Mach number on the plane wave scattering of the long cavity filled with aluminum foam and with the locally-resonant metamaterial.

Fig. 22a,b show the scattering coefficients of the long porous cavity. The effect of M on the transmission coefficients is simple: a small and approximately uniform increase of $|T^{+}|$, and a small and approximately uniform decrease of $|T^{-}|$. The effect on the reflection coefficients is similar concerning the levels, i.e. $|R^{+}|$ augments and $|R^{-}|$ diminishes. But also, it is observed that the peaks of $|R^{\pm}|$ shift to lower frequencies. The reason is that for the short cavity the peaks are associated to cavity resonances in the direction normal to the duct, so that the change in axial wavelength of the plane waves in the main duct doesn't change the resonant frequencies. On the other hand, the peaks in $|R^{\pm}|$ of the long cavity are associated to axial resonances of the cavity, which are more sensitive to the wavelength of the plane waves in the main duct and thus to M.

In the case of the long cavity filled with locally-resonant metamaterial the behavior is quite different overall (see Fig. 22c,d). Increasing M causes a slight shift of both $|T^{+}|$ and $|T^{-}|$ to higher frequencies, with almost no effect on the overall trend or the levels, even for the highest frequency. The effect on the reflection coefficients is larger, and much more similar to the case of the porous liners, i.e. increasing M causes an approximately uniform increase of $|R^{+}|$ and a decrease

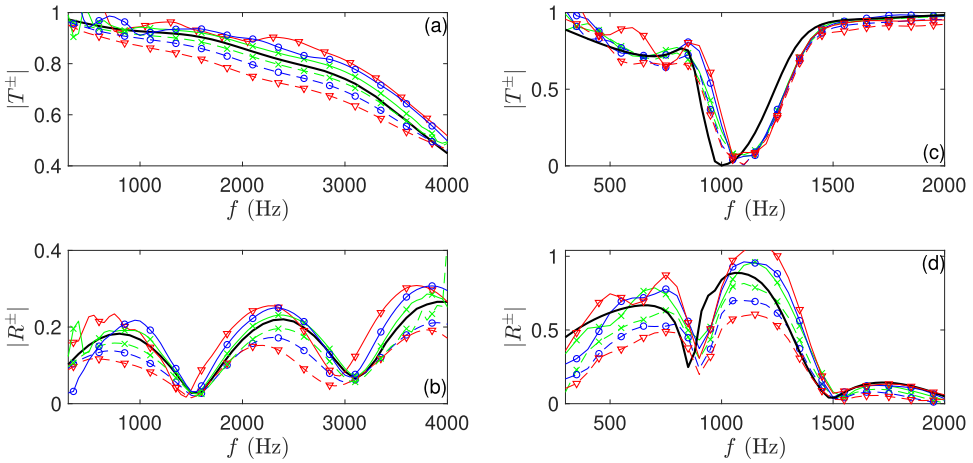

Fig. 22. $|T|, |R|$ at $M = 0$ (——), $|T^+|, |R^+|$ at $M = 0.1$ (—×—), $M = 0.2$ (—○—) and $M = 0.3$ (—▽—), $|T^-|, |R^-|$ at $M = 0.1$ (- × -), $M = 0.2$ (- ○ -) and $M = 0.3$ (- ▽ -), for the long cavity filled with aluminum foam (a,b) and with the locally-resonant metamaterial (c,d).

of $|R^-|$. The good performance of the metamaterial-based liner with flow which acts as a sound barrier around the resonance frequency, for both upstream and downstream sources, illustrates the potential of this type of material in aeroacoustic applications.

7. Conclusions

In this study a full FDTD methodology to compute the acoustic field of a flow duct treated with general extended-reacting liners, including a perforated sheet, has been introduced and validated. The liner material is treated as an equivalent fluid, and the ADE method is used to substitute the convolution integrals that appear in the time-domain equations by a set of auxiliary differential equations which can be solved simultaneously to the mass and momentum equations, allowing the use of high-order spatial and temporal schemes. Its use has been illustrated for rigid-frame porous materials and a simple prototype of effective medium for a locally-resonant metamaterial. While simulations have been performed for 2D geometries, the extension to the 3D case is straightforward.

In a first stage the FDTD algorithm has been validated against the analytical solution in a 1D configuration, corresponding to reflexion and transmission at an interface with a semi-infinite liner. The various contributions to the total error have been highlighted: the truncation of the partial fraction expansion of the effective density and compressibility, the truncation of the partial fraction expansions involved in a general broadband interface condition, and finally the pure numerical error. The latter dominates the total error as long as the number of poles retained is high enough, and follows the expected order of the numerical schemes used.

In a second stage, the FDTD algorithm has been applied to a 2D flow duct treated with extended-reacting liners, and successfully validated against experimental results of porous liners with and without flow. The GTS method has been shown to be effective at suppressing the hydrodynamic instability, with only a small impact on the acoustic component. Interesting features in the performance of liners based on a locally-resonant metamaterial have been identified which illustrate their potential in this application. In particular, it has been shown that the transmission coefficient of metamaterial-based liners in the presence of a mean flow remains low and close to the no-flow transmission coefficient around the leading resonance frequency of the metamaterial. Furthermore, it appears that around this frequency the liner behaves closely to its locally-reacting counterpart. This might allow designing these liners around the resonance using their locally-reacting approximation, i.e. directly through their impedance.

Future work will focus on the development of metamaterials for lined duct flow applications and on their modeling for time-domain simulations. In addition, the proposed treatment of the interface could also be used to investigate the attenuation due to empty cavities lined by a perforated plate, for which extensive experimental data are available [63].

Declaration of Competing Interest

The authors declare that they have no known competing financial interests or personal relationships that could have appeared to influence the work reported in this paper.

CRediT authorship contribution statement

Antoni Alomar: Investigation, Writing - original draft, Methodology. **Didier Dragna:** Investigation, Writing - original draft, Methodology, Writing - review & editing. **Marie-Annick Galland:** Investigation, Writing - original draft, Writing - review & editing.

Acknowledgements

This work was performed within the framework of the Labex CeLyA of the University of Lyon, within the program "Investissements d'Avenir" (ANR-10-LABX-0060/ANR-16-IDEX-0005) operated by the French National Research Agency. The authors would like to acknowledge the financial support from the European Union's Horizon 2020 research and innovation program through the ARTEM project under grant No 769 350.

Appendix A. Johnson-Champoux-Allard-Pride-Lafarge model

The JCAPL semi-phenomenological model [46] describes a large family of rigid-frame porous media. The effective density and effective compressibility, in the equivalent fluid formulation, are fully characterized by 8 parameters: the porosity (ϕ), the tortuosity (α_∞), the viscous length (Λ), the thermal length (Λ'), the viscous permeability (k_0), the thermal permeability (k_0'), the static viscous tortuosity (α_0), and the static thermal tortuosity (α_0'):

$$\frac{\rho_e(\omega)}{\rho_0} = \frac{1}{\phi}\left(\alpha_\infty + \frac{1}{\mathrm{j}X}\left(\sqrt{\mathrm{j}MN^2 + b^2} - b + 1\right)\right), \tag{A.1a}$$

$$\rho_0 c_0^2 C_e(\omega) = \phi\left(\gamma - \frac{\gamma - 1}{C}\right), \quad C = 1 + \frac{1}{\mathrm{j}X'}\left(\sqrt{\mathrm{j}M'(N')^2 + (b')^2} - b' + 1\right), \tag{A.1b}$$

$$b = \frac{2\alpha_\infty^2 k_0}{\Lambda^2 \phi(\alpha_0 - \alpha_\infty)}, \quad b' = \frac{2k_0'}{(\Lambda')^2 \phi(\alpha_0' - 1)}, \tag{A.1c}$$

$$X = \frac{\omega\rho_0 k_0}{\mu_0 \phi}, \quad X' = \frac{\omega\rho_0 k_0' Pr}{\mu\phi}, \tag{A.1d}$$

$$M = \frac{\omega\rho_0}{\mu_0}, \quad M' = \frac{\omega\rho_0 Pr}{\mu}, \tag{A.1e}$$

$$N = \frac{2\alpha_\infty k_0}{\Lambda\phi}, \quad N' = \frac{2k_0'}{\Lambda'\phi}, \tag{A.1f}$$

The full JCAPL model reduces to the Johnson-Champoux-Allard-Lafarge model (JCAL) by setting $b = b' = 1$, and the Johnson-Champoux-Allard model (JCA) is obtained by setting $k_0' = \phi\Lambda'^2/8$.

Appendix B. Analytical solution for the reflection and the transmission of a plane wave pulse at an interface between two semi-infinite fluid media

Details on the analytical solution for the transmission and reflection of an acoustic pulse at an interface between air and a sound-absorbing material in the form of an equivalent fluid are given here.

In air ($x > 0$), the pressure can be written in the time domain as:

$$p_{\mathrm{ana}}^a(x,t) = p_0(x - x_s + c_0 t) + [r * p_0](x + x_s - c_0 t) \tag{B.1}$$

where the first contribution corresponds to the incident pulse traveling leftwards and the second contribution to the reflected pulse at the interface, traveling rightwards. The operator $*$ denotes convolution and $r(t)$ is the impulse response associated to the reflection coefficient. Eq. B.1 can also be written as the inverse Fourier transform

$$p_{\mathrm{ana}}^a(x,t) = \frac{1}{2\pi}\int_{-\infty}^{+\infty} \frac{1}{c_0}\hat{p}_0(k_0)\left(\mathrm{e}^{\mathrm{j}k_0(x-x_s)} + R(\omega)\,\mathrm{e}^{-\mathrm{j}k_0(x+x_s)}\right)\mathrm{e}^{\mathrm{j}\omega t}\mathrm{d}\omega. \tag{B.2}$$

In the above expression, $k_0 = \omega/c_0$ is the wavenumber in air and R is the reflection coefficient:

$$R(\omega) = \frac{Z_e(\omega) + Z_{sh}(\omega) - \rho_0 c_0}{Z_e(\omega) + Z_{sh}(\omega) + \rho_0 c_0}, \tag{B.3}$$

where $Z_e(\omega) = \sqrt{\rho_e(\omega)/C_e(\omega)}$ is the characteristic impedance of the material and $Z_{sh}(\omega)$ accounts for a possible pressure jump at the interface, due e.g. to a resistive screen or a perforated plate. Finally, $\hat{p}_0$ is the Fourier transform of the incident pulse:

$$\hat{p}_0(k) = \int_{-\infty}^{\infty} p_0(x)\, \mathrm{e}^{-\mathrm{j}kx} \mathrm{d}x, \tag{B.4}$$

which, for the Mexican hat used in this study, is given by:

$$\hat{p}_0(k) = \sqrt{2\pi} B (kB)^2 \exp\left(-\frac{k^2 B^2}{2}\right). \tag{B.5}$$

In the sound-absorbing material ($x < 0$), the pressure of the pulse transmitted through the interface can be expressed as the following inverse Fourier transform:

$$p^m_{\mathrm{ana}}(x,t) = \frac{1}{2\pi} \int_{-\infty}^{+\infty} \frac{1}{c_0} \hat{p}_0(k_0)\, \mathrm{e}^{-\mathrm{j}k_0 x_s} T(\omega)\, \mathrm{e}^{\mathrm{j}k_e x} \mathrm{e}^{\mathrm{j}\omega t} \mathrm{d}\omega \tag{B.6}$$

where $k_e(\omega) = \omega\sqrt{\rho_e(\omega) C_e(\omega)}$ is the wavenumber in the material and $T(\omega)$ is the transmission coefficient, given by:

$$T(\omega) = \frac{2 Z_e(\omega)}{Z_e(\omega) + Z_{sh}(\omega) + \rho_0 c_0} \tag{B.7}$$

Appendix C. Determination of the scattering matrix from the time-domain simulations

The plane wave scattering matrix is determined from the time signals of 2 pressure sensors upstream and 2 pressure sensors downstream, corresponding to two different source configurations: a downstream source (I) and an upstream source (II). The four complex equations (one for each pair of sensors and each source configuration) can be re-arranged into the following matrix system:

$$\begin{pmatrix} R_1^I & T_{21}^{II} \\ T_{12}^I & R_2^{II} \end{pmatrix} = \begin{pmatrix} R^+ & T^- \\ T^+ & R^- \end{pmatrix} \begin{pmatrix} I & \frac{R_2^{II}}{T_{12}^{II}} \\ \frac{T_{12}^I}{R_2^I} & I \end{pmatrix}, \tag{C.1}$$

where

$$R_1 = \frac{\hat{p}_1^-}{\hat{p}_1^+} = \frac{H_{12,u}\exp(-jk_0^+ x_{1u}) - \exp(-jk_0^+ x_{2u})}{\exp(jk_0^- x_{1u}) - H_{12,u}\exp(jk_0^- x_{2u})},$$

$$R_2 = \frac{\hat{p}_2^+}{\hat{p}_2^-} = \frac{H_{12,d}\exp(jk_0^- x_{2d}) - \exp(jk_0^- x_{1d})}{\exp(-jk_0^+ x_{1d}) - H_{12,d}\exp(-jk_0^+ x_{2d})},$$

$$T_{12} = \frac{\hat{p}_2^+}{\hat{p}_1^+} = H_{11,du}\frac{\exp(-jk_0^+ x_{1u}) + R_1\exp(jk_0^- x_{1u})}{\exp(-jk_0^+ x_{1d}) + (1/R_2)\exp(jk_0^- x_{1d})},$$

$$T_{21} = \frac{\hat{p}_1^-}{\hat{p}_2^-} = H_{11,ud}\frac{R_2\exp(-jk_0^+ x_{1d}) + \exp(jk_0^- x_{1d})}{(1/R_1)\exp(-jk_0^+ x_{1u}) + \exp(jk_0^- x_{1u})},$$

$$H_{12,u} = \frac{\hat{p}_{x_1 u}}{\hat{p}_{x_2 u}}, \quad H_{12,d} = \frac{\hat{p}_{x_1 d}}{\hat{p}_{x_2 d}}, \quad H_{11,du} = \frac{\hat{p}_{x_1 d}}{\hat{p}_{x_1 u}}, \quad H_{11,ud} = \frac{\hat{p}_{x_1 u}}{\hat{p}_{x_1 d}},$$

where the downstream and upstream wavenumbers are defined as

$$k_0^+ = \frac{\omega}{c_0(1+M)}, \quad k_0^- = \frac{\omega}{c_0(1-M)}.$$

The linear system (C.1) is solved successively for all frequencies.

Supplementary material

Supplementary material associated with this article can be found, in the online version, at doi:10.1016/j.jsv.2021.116137.

References

[1] F. Paun, S. Gasser, L. Leylekian, Design of materials for noise reduction in aircraft engines, Aerosp. Sci. Technol. 7 (2003) 63–72.
[2] D. Sutliff, M. Jones, Low-speed fan noise attenuation from a foam-metal liner, J. Aircr. 46 (2009) 1381–1394.
[3] M.G. Jones, B.M. Howerton, Evaluation of novel liner concepts for fan and airframe noise reduction, in: 22nd AIAA/CEAS Aeroacoustics Conference, Lyon, France, 30 May - 1 June 2016, AIAA 2016-2787, p.1-18.
[4] B.S. Beck, N.H. Schiller, M.G. Jones, Impedance assessment of a dual-resonance acoustic liner, Appl. Acoust. 93 (2015) 15–22.
[5] G. Palma, H. Mao, L. Burghignoli, P. Göransson, U. Iemma, Acoustic metamaterials in aeronautics, Appl. Sci. 8 (971) (2018).
[6] L. Xiong, B. Nennig, Y. Aurégan, W. Bi, Sound attenuation optimization using metaporous materials tuned on exceptional points, J. Acoust. Soc. Am. 142 (4) (2017) 2288–2297.

[7] H. Utsuno, T.W. Wu, A.F. Seybert, T. Tanaka, Prediction of sound fields in cavities with sound absorbing materials, AIAA J. 28 (11) (1990) 1870–1876.
[8] R.J. Astley, A. Cummings, N. Sormaz, A finite element scheme for acoustic propagation in flexible-walled ducts with bulk-reacting liners, and comparison with experiment, J. Sound Vibr. 150 (1991) 119–138.
[9] R. Kirby, J.B. Lawrie, A point collocation approach to modeling large dissipative silencers, J. Sound Vibr. 286 (1–2) (2005) 313–339.
[10] A. Cummings, I.J. Chang, Sound attenuation of a finite length dissipative flow duct silencer with internal mean flow in the absorbent, J. Sound Vibr. 127 (1) (1988) 1–17.
[11] B. Nennig, E. Perrey-Debain, M.B. Tahar, A mode matching method for modeling dissipative silencers lined with poroelastic materials and containing mean flow, J. Acoust. Soc. Am. 128 (6) (2010) 3308–3320.
[12] C. Bogey, C. Bailly, A family of low dispersive and low dissipative explicit schemes for flow and noise computations, J. Comput. Phys. 194 (2004) 194–214.
[13] J. Berland, C. Bogey, O. Marsden, C. Bailly, High-order, low dispersive and low dissipative explicit schemes for multiple-scale and boundary problems, J. Comput. Phys. 224 (2) (2007) 637–662.
[14] J. Berland, C. Bogey, C. Bailly, Low-dissipation and low-dispersion fourth-order Runge–Kutta algorithm, Comput. Fluids 35 (2006) 1459–1463.
[15] C. Scalo, J. Bodart, S.K. Lele, Compressible turbulent channel flow with impedance boundary conditions, Physics Fluids 27 (2015) 035107,1–22.
[16] S. Olivetti, R.D. Sandberg, B.J. Tester, Direct numerical simulation of turbulent flow with an impedance condition, J. Sound Vibr. 344 (2015) 28–37.
[17] R. Sebastian, D. Marx, V. Fortuné, Numerical simulation of a turbulent channel flow with an acoustic liner, J. Sound Vibr. 456 (2019) 306–3330.
[18] Z.E.A. Fellah, C. Depollier, Transient acoustic wave propagation in rigid porous media: a time-domain approach, J. Acoust. Soc. Am. 107 (2) (2000) 683–688.
[19] C. Zwikker, C.W. Kosten, Sound Absorbing Materials, Elsevier, 1949.
[20] M.C. Berengier, M.R. Stinson, G.A. Daigle, J.F. Hamet, Porous road pavements: acoustical characterization and propagation effects, J. Acoust. Soc. Am. 101 (1997) 155–162.
[21] Y. Wang, K.M. Li, D. Dragna, P. Blanc-Benon, On the sound field from a source moving above non-locally reacting grounds, J. Sound Vib. 464 (2020) 1–20. 114975
[22] D.K. Wilson, V.E. Ostashev, S.L. Collier, N.P. Symons, D.F. Aldridge, D.H. Marlin, Time-domain calculations of sound interactions with outdoor ground surfaces, Appl. Acoust. 68 (2) (2007) 173–200.
[23] D.K. Wilson, Simple, relaxational models for the acoustical properties of porous media, Appl. Acoust. 50 (3) (1997) 171–188.
[24] O. Umnova, D. Turo, Time domain formulation of the equivalent fluid model for rigid porous media, J. Acoust. Soc. Am. 125 (4) (2009) 1860–1863.
[25] D.F. Kelley, R.J. Luebbers, Piecewise linear recursive convolution for dispersive media using FDTD, IEEE Trans. Antennas Propag. 44 (6) (1996) 792–797.
[26] D.M. Sullivan, Frequency-dependent FDTD methods using Z transforms, IEEE Trans. Antennas Propag. 40 (10) (1992) 1223–1230.
[27] R.M. Joseph, S.C. Hagness, A. Taflove, Direct time integration of Maxwell's equations in linear dispersive media with absorption for scattering and propagation of femtosecond electromagnetic pulses, Opt. Lett. 16 (18) (1991) 1412–1414.
[28] D. Dragna, P. Pineau, P. Blanc-Benon, A generalized recursive convolution method for time-domain propagation in porous media, J. Acoust. Soc. Am. 138 (2) (2015) 1030–1042.
[29] X. Zhao, M. Bao, X. Wang, H. Lee, S. Sakamoto, An equivalent fluid model based finite-difference time-domain algorithm for sound propagation in porous material with rigid frame, J. Acoust. Soc. Am. 143 (1) (2018) 130–138.
[30] C. Bellis, B. Lombard, Simulating transient wave phenomena in acoustic metamaterials using auxiliary fields, Wave Motion 86 (2019) 175–194.
[31] D.Y. Maa, Microperforated-panel wideband absorbers, Noise Control Eng. J. 29 (3) (1987) 77–84.
[32] A.B. Bauer, Impedance theory and measurements on porous acoustic liners, J. Aircr. 14 (8) (1977) 720–728.
[33] I.J. Hughes, A.P. Dowling, The absorption of sound by perforated linings, J. Fluid Mech. 218 (1990) 299–335.
[34] C. Lawn, The acoustic impedance of perforated plates under various flow conditions relating to combustion chamber liners, Appl. Acoust. 106 (2016) 144–154.
[35] C.K.W. Tam, L. Auriault, Time-domain impedance boundary conditions for computational aeroacoustics, AIAA J. 34 (5) (1996) 917–923.
[36] Y. Özyörük, L.N. Long, A time-domain implementation of surface acoustic impedance condition with and without flow, J. Comput. Acoust. 05 (03) (1997) 277–296.
[37] R. Troian, D. Dragna, C. Bailly, M.A. Galland, Broadband liner impedance eduction for multimodal acoustic propagation in the presence of a mean flow, J. Sound Vibr. 392 (2017) 200–216.
[38] B. Gustavsen, A. Semlyen, Rational approximation of frequency domain responses by vector fitting, IEEE Trans. Power Deliv. 14 (3) (1999) 1052–1061.
[39] K.V. Horoshenkov, K. Attenborough, S.N.C. Wilde, Padé approximants for the acoustical properties of rigid frame porous media with pore size distributions, J. Acoust. Soc. Am. 104 (3) (1998) 1198–1209.
[40] A. Alomar, D. Dragna, M.A. Galland, Pole identification method to extract the equivalent fluid characteristics of general sound-absorbing materials, Appl. Acoust. 174 (2021) 107752,1–15.
[41] H. Wang, J. Yang, M. Hornikx, Frequency-dependent transmission boundary condition in the acoustic time-domain nodal discontinuous Galerkin model, Appl. Acoust. 164 (2020) 1–13 107280.
[42] C. Bogey, N. de Cacqueray, C. Bailly, A shock-capturing methodology based on adaptative spatial filtering for high-order non-linear computations, J. Comput. Phys. 228 (5) (2009) 1447–1465.
[43] C.K.W. Tam, Z. Dong, Radiation and outflow boundary conditions for direct computation of acoustic and flow disturbances in a nonuniform mean flow, J. Comput. Acoust. 04 (02) (1996) 175–201.
[44] C. Bogey, C. Bailly, Three-dimensional non-reflective boundary conditions for acoustic simulations: far field formulation and validation test cases, Acta Acust. united Acust. 88 (4) (2002) 463–471.
[45] R.J. LeVeque, Finite Difference Methods for Ordinary and Partial Differential Equations: Steady-State and Time-Dependent Problems, first edition, SIAM, Philadelphia, PA, 2007.
[46] J.F. Allard, N. Atalla, Propagation of Sound in Porous Media: Modelling Sound Absorbing Materials, second ed., John Wiley & Sons, Chichester, West Sussex, 2009, p. 90.
[47] Z. Liu, X. Zhang, Y. Mao, Y.Y. Zhu, Z. Yang, C.T. Chan, P. Sheng, Locally resonant sonic materials, Science 289 (5485) (2000) 1734–1736.
[48] D.R. Smith, S. Schultz, P. Markoc, C.M. Soukoulis, Determination of effective permittivity and permeability of metamaterials from reflection and transmission coefficients, Phys. Rev. B 65 (2002) 195104.
[49] D. Felbacq, G. Bouchitté, Theory of mesoscopic magnetism in photonic crystals, Phys. Rev. Lett. 94 (2005).
[50] N. Fang, D. Xi, J. Xu, M. Ambati, W. Srituravanich, C. Sun, X. Zhang, Ultrasonic metamaterials with negative modulus, Nat. Mater. 5 (6) (2006) 452.
[51] V. Romero-Garcia, A. Krynkin, L.M. Garcia-Raffi, O. Umnova, J.V. Sanchez-Perez, Multi-resonant scatterers in sonic crystals: locally multi-resonant acoustic metamaterial, J. Sound Vibr. 332 (1) (2013) 184–198.
[52] D.Y. Maa, Theory and design of microperforated panel sound-absorbing constructions, Scientia Sinica 18 (1) (1975) 55–71.
[53] G. Ajello, Mesures acoustiques dans les guides d'ondes en présence d'écoulement : Mise au point d'un banc de mesure, application à des discontinuités, Université du Maine, 1997 Ph.D. thesis.
[54] Y. Aurégan, M. Leroux, V. Pagneux, Measurement of liner impedance with flow by an inverse method, in:10th AIAA/CEAS Aeroacoustics Conference, Manchester, Great-Britain, 10-12 May 2004, AIAA 2004-2838, p.1-7.
[55] D. Marx, Y. Aurégan, H. Bailliet, J.-C. Valière, PIV and LDV evidence of hydrodynamic instability over a liner in a duct with flow, J. Sound Vibr. 329 (2010) 3798–3812.
[56] A. Alomar, Y. Aurégan, Particle image velocimetry measurement of an instability wave over a porous wall in a duct with flow, J. Sound Vibr. 386 (2017) 208–224.

[57] E.J. Brambley, G. Gabard, Time-domain implementation of an impedance boundary condition with boundary layer correction, J. Comput. Phys. 321 (2016) 755–775.
[58] D. Marx, Y. Aurégan, Effect of turbulent eddy viscosity on the unstable surface mode above an acoustic liner, J. Sound Vibr. 332 (2013) 3803–3820.
[59] C. Bogey, C. Bailly, D. Juvé, Computation of flow noise using source terms in linearized Euler's equations, AIAA J. 40 (2) (2002) 235–243.
[60] Y. Sun, R. Fattah, S. Zhong, X. Zhang, Stable time-domain CAA simulations with linearised governing equations, Comput. Fluids 167 (2018) 187–195.
[61] Y. Deng, A. Alomar, D. Dragna, M.A. Galland, Characterization and suppression of the hydrodynamic instability in the time domain for acoustic propagation in a lined flow duct, J. Sound Vibr. 500 (2021) 115999,1–22.
[62] Y. Aurégan, D.K. Singh, Experimental observation of a hydrodynamic mode in a flow duct with a porous material, J. Acoust. Soc. Am. 136 (2) (2014) 567–572.
[63] C. Lahiri, L. Enghardt, F. Bake, S. Sadig, M. Gerendás, Establishment of a high quality database for the acoustic modeling of perforated liners, J. Eng. Gas Turbines Power 133 (2011) 091503,1–9.